

Estimating T_{eff} , radius and luminosity of M-dwarfs using high resolution optical and NIR spectral features

Dhrimadri Khata,¹[★](#) Soumen Mondal,¹ Ramkrishna Das,¹ Tapas Baug¹

¹Satyendra Nath Bose National Centre for Basic Sciences, Block-JD, Sector-III, Salt Lake, Kolkata-700 106

Accepted XXX. Received YYY; in original form ZZZ

ABSTRACT

We estimate effective temperature (T_{eff}), stellar radius, and luminosity for a sample of 271 M-dwarf stars (M0V–M7V) observed as a part of CARMENES (Calar Alto high-Resolution search for M dwarfs with Exo-earths with Near-infrared and optical Echelle Spectrographs) radial-velocity planet survey. For the first time, using the simultaneously observed high resolution ($R \sim 90000$) spectra in the optical (0.52–0.96 μm) and near-infrared (0.96–1.71 μm) bands, we derive empirical calibration relationships to estimate the fundamental parameters of these low-mass stars. We select a sample of nearby and bright M-dwarfs as our calibrators for which the physical parameters are acquired from high-precision interferometric measurements. To identify the most suitable indicators of T_{eff} , radius, and luminosity ($\log L/L_{\odot}$), we inspect a range of spectral features and assess them for reliable correlations. We perform multivariate linear regression and find that the combination of pseudo equivalent widths and equivalent width ratios of the Ca II at 0.854 μm and Ca II at 0.866 μm lines in the optical and the Mg I line at 1.57 μm in the NIR give the best fitting linear functional relations for the stellar parameters with root mean square errors (RMSE) of 99K, 0.06 R_{\odot} and 0.22 dex respectively. We also explore and compare our results with literature values obtained using other different methods for the same sample of M dwarfs.

Key words: stars:fundamental parameters – stars:low-mass – techniques:spectroscopic – methods:observational.

1 INTRODUCTION :

The properties of planets are directly connected with the fundamental physical properties of the host stars (Santos et al. 2004; Mann et al. 2013b). The small size, low mass range (0.075–0.50 M_{\odot}), Delfosse et al. 2000), presence of protoplanetary disks (Laughlin et al. 2004, Mercer & Stamatellos 2020) and chemically rich environment (Ida & Lin 2004) of M-dwarf stars make them prime targets for exoplanet and brown dwarf searches (Bonfils et al. 2013; Anglada-Escudé et al. 2016). The photometric transit of a planet helps to measure the planet to star radius ratio, and the radial velocity or astrometry wobbles of a star allows to determine the planet to star mass ratio. Though the intrinsic faintness and variation of the properties across all M-spectral subtypes make the task challenging, the precise estimation of the stellar parameters of M dwarfs is extremely important in many aspects of stellar and galactic astronomy: understanding the chemical evolution and star-formation history (Bochanski et al. 2007), tracing the galactic disc kinematics (e.g., Hawley, Gizis & Reid 1996; Reid, Gizis & Hawley 2002), studying stellar age-velocity relations (West et al. 2006), constraining galactic structure (e.g., Reid et al. 1997; Pirzkal et al. 2005) and the galaxy’s mass and luminosity (e.g., Hawkins & Bessell 1988;

Kirkpatrick et al. 1994; Zheng et al. 2001, 2004).

Earlier work constraining the effective temperature (T_{eff}) of M dwarfs has been carried out using photometry (Leggett et al. 1996) and blackbody fitting techniques (Bessell 1991). The straightforward way to derive the T_{eff} is by using the angular diameter estimated from stellar evolution tracks through interferometry (Boyajian et al. 2012), and bolometric flux obtained from multi-band photometry (Nordström et al. ?). Another method to determine the parameters is by comparing M dwarf spectra with synthetic models for cool stellar atmospheres (i.e., Casagrande et al. 2008; Gaidos 2013; Dressing & Charbonneau 2013). Veyette et al. (2017) and Rajpurohit et al. (2018) used advanced BT-Settl models (Allard et al. 2012, 2013) to determine the stellar parameters of M dwarfs using CARMENES high resolution spectra (Reiners et al. 2018). However, the formation of molecules and dust grains due to cool temperature and inaccurate modeling of the magnetic field induced by the deep convective zones in M dwarf interiors (Mullan & MacDonald 2001; Browning 2008), constrain the accuracy of theoretical model predictions.

As the direct measurement of the stellar radius is limited to few nearby bright M dwarfs (Berger et al. 2006), empirical calibrations can be determined and applied to other M dwarfs. Ballard et al. (2013) used interferometric radii to constrain the T_{eff} and radius of Kepler-61b; Boyajian et al. (2012) calculated radii for K- and M-

* E-mail: dhrimadrikht@gmail.com (DK)

stars using a mass-radius relation; Johnson et al. (2012) constrained the mass and radius for Kepler Object of Interest (KOI) 254. To derive the metallicity calibration relations for M dwarfs, the use of an F, G, or K binary companion with known metallicity is a well adopted method both in spectroscopy (Newton et al. 2014; Mann et al. 2013a) and in photometry (Bonfils et al. 2005; Casagrande et al. 2008; Schlaufman & Laughlin 2010). More recently machine learning techniques have been applied widely, where different neural network architectures are built and trained to determine stellar parameters of M dwarfs (Sarro et al. 2018, Sharma et al. 2019, Antoniadis-Karnavas et al. 2020, Passegger et al. 2020).

The measurement and identification of pseudo equivalent widths (pEWs) and spectral indices of various atomic and molecular features in the optical and NIR bands that are sensitive to different stellar parameters, can also be used as an effective alternative approach to obtain cool star's physical parameters. This method has been widely applied to M dwarfs by Mann, Gaidos & Ansdell (2013b) and Newton et al. (2015) to estimate effective temperature, radius, and luminosity. The M dwarf's T_{eff} -scale was defined using optical TiO, VO, CrH, FeH equivalent widths by Tinney & Reid (1998) and using NIR H_2O indices by Delfosse et al. (1999). Rojas-Ayala et al. (2012) estimated spectral-type and T_{eff} using the K-band H_2O index and metallicity using pEWs of the K-band Na I and Ca I features along with the H_2O index. Khata et al. (2020) applied the H_2O -H index defined by Terrien et al. (2012) in the NIR calibration relations of T_{eff} and radius for M dwarfs and evaluated the spectral type and absolute K_s magnitude as a linear function of both H- and K-band H_2O indices. Also, Neves et al. (2012, 2013) used pEWs to estimate metallicity and T_{eff} for M dwarfs, and Woolf & Wallerstein (2006) derived CaH and TiO molecular indices to estimate metallicities of K- and M-dwarfs.

With the development of high-resolution spectrographs, spectra of distant and faint M dwarfs with good signal-to-noise ratio has become available both in the optical (i.e., HARPS, Mayor et al. 2003; HARPS-N, Cosentino et al. 2012) and in the NIR wavelength (CRIRES, Kaeufl et al. 2004). The CARMENES (Reiners et al. 2018) radial velocity survey offers an atlas of high resolution ($R > 80000$) M dwarf spectra abundant with numerous features simultaneously observed in the optical and NIR from 520–1710 nm (where M dwarfs emit maximum flux). To minimize trend degeneracies and biases due to M dwarf environment, the simultaneous use of equivalent widths from the optical and NIR is proving very fruitful. As the EWs of the lines with higher excitation potential (χ) change faster with temperature than those with lower excitation potential (Gray 1994), the ratio of such EWs that have different temperature sensitivity have been extensively used as T_{eff} indicators for solar-type stars (i.e. Gray 1994; Kovtyukh et al. 2003; Montes et al. 2006; Sousa et al. 2010), giant type stars (i.e. Gray 1989; Strassmeier & Schordan 2000) and for super-giants (i.e. Kovtyukh & Gorlova 2000). The benefit of estimating stellar parameters using the EW ratios is that it is independent of the effect of interstellar reddening, spectral resolution, rotational and microturbulence broadening (Kovtyukh et al. 2003).

In this paper, we estimate T_{eff} , radius and luminosity using sensitive pseudo-EWs and EW ratios from the optical and NIR for a sample of 271 M dwarfs. Though good parallax measurements are available from the Gaia DR2 and Gaia EDR3 catalog (Gaia Collaboration et al. 2018 & 2021) for our selected CARMENES sample of potential planet-hosting M dwarfs (except one object, 2M J06572616+7405265), the parameters estimated from the spectral features are proven to be strikingly useful. The Spectroscopic data is obtained from the CARMENES radial velocity (RV) survey,

which observed 324 M dwarfs during guaranteed time observations (GTO) to search for any orbiting planets.

2 DATA ACQUISITION & CALIBRATORS SELECTION:

We worked with a sample of 271 bright, nearby M-dwarfs with a good signal-to-noise ratio ($S/N > 75$) across all M-spectral subtypes (M0V-M7V), based on data from the CARMENES data archive at CAB (INTA-CSIC)¹ (Reiners et al. 2018). The spectrograph, installed on the Zeiss 3.5 m telescope, is located at Calar Alto observatory in Spain, and the data was reduced using an automatic pipeline (Zechmeister et al. 2014) and more details are given in Caballero et al. (2016) and Nidever et al. (2015). CARMENES provides a wide range of high resolution spectra both in the optical channel with wavelength from 0.52–0.96 μm and spectral resolution, $R \sim 94600$; and in the NIR channel with wavelength from 0.96–1.71 μm and resolution, $R \sim 80400$. After rejecting several double-lined spectroscopic binaries (SB2s), Reiners et al. (2018) came up with an initial sample of 324 M-dwarfs with an average age of 5 Gyr (Cortés-Contreras et al. 2017; Passegger et al. 2018) and a typical limit for the J-band magnitude ($m_J = 10$ mag). From this sample, we selected mainly isolated M dwarfs or those having widely separated ($> 5''$) companions and ruled out the fast rotators and stars with signatures of activity that affect the profiles of the spectral lines (Passegger et al. 2018; Schweitzer et al. 2019).

We choose a sample of 23 target stars with high precision long-baseline interferometric measurements of radii (Boyajian et al. 2012; Mann et al. 2015; Markus Rabus et al. 2019) for the calibration of stellar parameters. We preferably select 13 calibrators from Newton et al. (2015) where the bolometric luminosities (L_{bol}) are measured from multicolor photometry (Boyajian et al. 2012) and effective temperatures are calculated using the interferometric radius and bolometric flux (Mann et al. 2013b). We supplement this calibration sample with 6 M-dwarfs taken from Mann et al. (2015), where the bolometric flux (F_{bol}) was calculated by integrating over the radiative flux density and T_{eff} was calculated by fitting the optical spectra with the PHOENIX (BT-Settl) models (Allard et al. 2013). The remaining 4 calibrators were selected from Markus Rabus et al. (2019), where they estimated the F_{bol} using PHOENIX models (Husser et al. 2013) along with photometric observations and T_{eff} using the Stefan-Boltzmann law. The measured parameter values of our calibration sample cover T_{eff} from 2930 K to 4054 K, stellar radius from $0.183 R_{\odot}$ to $0.608 R_{\odot}$ and bolometric luminosity ($\log L/L_{\odot}$) from -2.625 to -1.048.

3 RESULT AND DISCUSSION :

3.1 Spectroscopic Analysis : Optical and NIR EW estimation

The presence of broad and complex molecular absorption bands in the optical (TiO, VO, CaH) and NIR (H_2O , FeH, CO, OH) over the entire spectral sequence of M dwarfs, make it difficult to identify the weak atomic lines in the spectra. The atomic features, such as Ti I (0.844 μm), Ca II (0.850 μm , 0.854 μm , 0.866 μm), Mg I (0.881 μm) in the optical band and the lines Ca I (1.035 μm), Na I (1.141 μm), K I (1.169 μm , 1.240 μm , 1.250 μm), Mg I (1.570 μm) in the NIR are strong enough and comparatively free from any

¹ <http://carmenes.cab.inta-csic.es/gto/jsp/reinersetal2018.jsp>

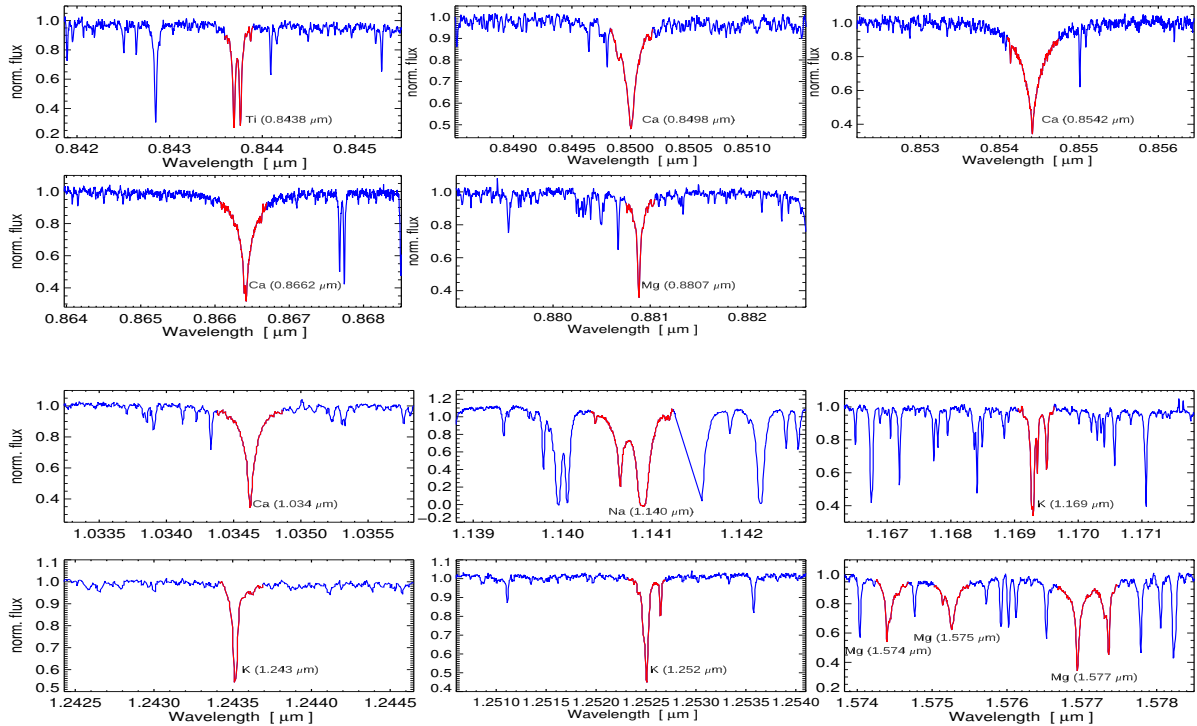


Figure 1. A representation of atomic absorption features in optical (Ti I [0.844 μm], Ca II [0.850 μm , 0.854 μm , 0.866 μm], Mg I [0.881 μm]) and Near-infrared (Ca I [1.035 μm], Na I [1.141 μm], K I [1.169 μm , 1.240 μm , 1.250 μm], Mg I [1.570 μm]) for the CARMENES spectra of the M-Dwarf GJ 2 (J00051+457) of spectral type M1.0V. We have calculated the EWs of these features with the feature window shown in red color to find and establish the strongest correlations with the stellar parameters.

blends and telluric contaminations. These spectral features are ideal tracers of T_{eff} , radius, and luminosity as the line strengths or equivalent widths depend on these stellar parameters (Rajpurohit et al. 2018; Newton et al. 2015). In Fig. 1 we show a representation of the absorption lines in the CARMENES spectra of the object GJ 2 (J00051+457) with the feature window colored in red. Some of the NIR atomic absorption features and indices that show significant correlation with stellar properties like Mg I at 1.50 μm , Al I at 1.67 μm , Mg I at 1.71 μm and H_2O -H index defined from 1.595 μm to 1.780 μm (Newton et al. 2015; Khata et al. 2020) are absent in the analysis as they are completely or partially in the gap of the CARMENES spectral format. In the J-band region, from 1.20 μm to 1.48 μm , the two K I lines at 1.243 μm and 1.252 μm stand out prominently, but the rest of this region is very poor in absorption lines due to wide molecular absorptions, telluric O_2 absorption and strong H_2O opacity. We have measured the EWs of the selected lines using the standard equation :

$$EW_{\lambda} = \int_{\lambda_1}^{\lambda_2} [1 - \frac{F(\lambda)}{F_c(\lambda)}] d\lambda \quad (1)$$

Here, $F(\lambda)$ represents the flux across the wavelength range of the line ($\lambda_2 - \lambda_1$), and $F_c(\lambda)$ stands for the estimated continuum flux on either side of the absorption line. The EWs are estimated using the modified versions of the publicly available IDL-based `tellrv`² and `nirew`³ packages originally developed by Newton et al. (2014, 2015). M dwarf's spectra are typically polluted by broad absorption

Table 1. Optical and NIR spectral features and continuum points

Feature	Feature window (μm)	Blue Continuum (μm)	Red Continuum (μm)
Ti I (0.844 μm) ^a	0.8436 0.8440	0.8431 0.8436	0.8443 0.8448
Ca II (0.850 μm) ^a	0.8498 0.8504	0.8485 0.8496	0.8504 0.8512
Ca II (0.854 μm) ^a	0.8540 0.8550	0.8530 0.8539	0.8552 0.8560
Ca II (0.866 μm) ^a	0.8660 0.8670	0.8650 0.8660	0.8670 0.8676
Mg I (0.881 μm) ^a	0.8808 0.8812	0.8798 0.8803	0.8815 0.8822
Ca I (1.034 μm) ^a	1.0343 1.0350	1.0335 1.0341	1.0352 1.0358
Na I (1.140 μm) ^b	1.1404 1.1413	1.1389 1.1397	1.1425 1.1434
K I (1.169 μm) ^b	1.1691 1.1697	1.1686 1.1691	1.1697 1.1705
K I (1.243 μm) ^b	1.2433 1.2438	1.2427 1.2433	1.2438 1.2444
K I (1.252 μm) ^b	1.2523 1.2528	1.2513 1.2520	1.2529 1.2535
Mg I (1.574 μm) ^b	1.5740 1.5780	1.5720 1.5740	1.5780 1.5800

Notes. Wavelengths are given in vacuum; ^(a) Atomic features are identified in Reiners et al. (2018), feature and continuum windows are defined based on our observations; ^(b) Feature and continuum windows are modified from those defined in Newton et al. (2015)

features or affected by extinction and contributions from emission sources such as hot dust. So based on our observation, we selected a pseudo continuum for each atomic feature by linear interpolation between adjacent regions, roughly 0.001–0.0015 μm wide on each side of the absorption line. The features and the continuum points used to calculate the equivalent widths are given in Table 1. The CARMENES high-resolution spectra show all three components of the NIR Mg I triplet (1.5740 μm , 1.5748 μm , 1.5765 μm), and as our continuum window covers all the components, they jointly contribute to the EW estimation of the Mg I (1.57 μm) feature. We have estimated the uncertainties on the EWs using a Monte

² <https://github.com/ernewton/tellrv>

³ <https://github.com/ernewton/nirew>

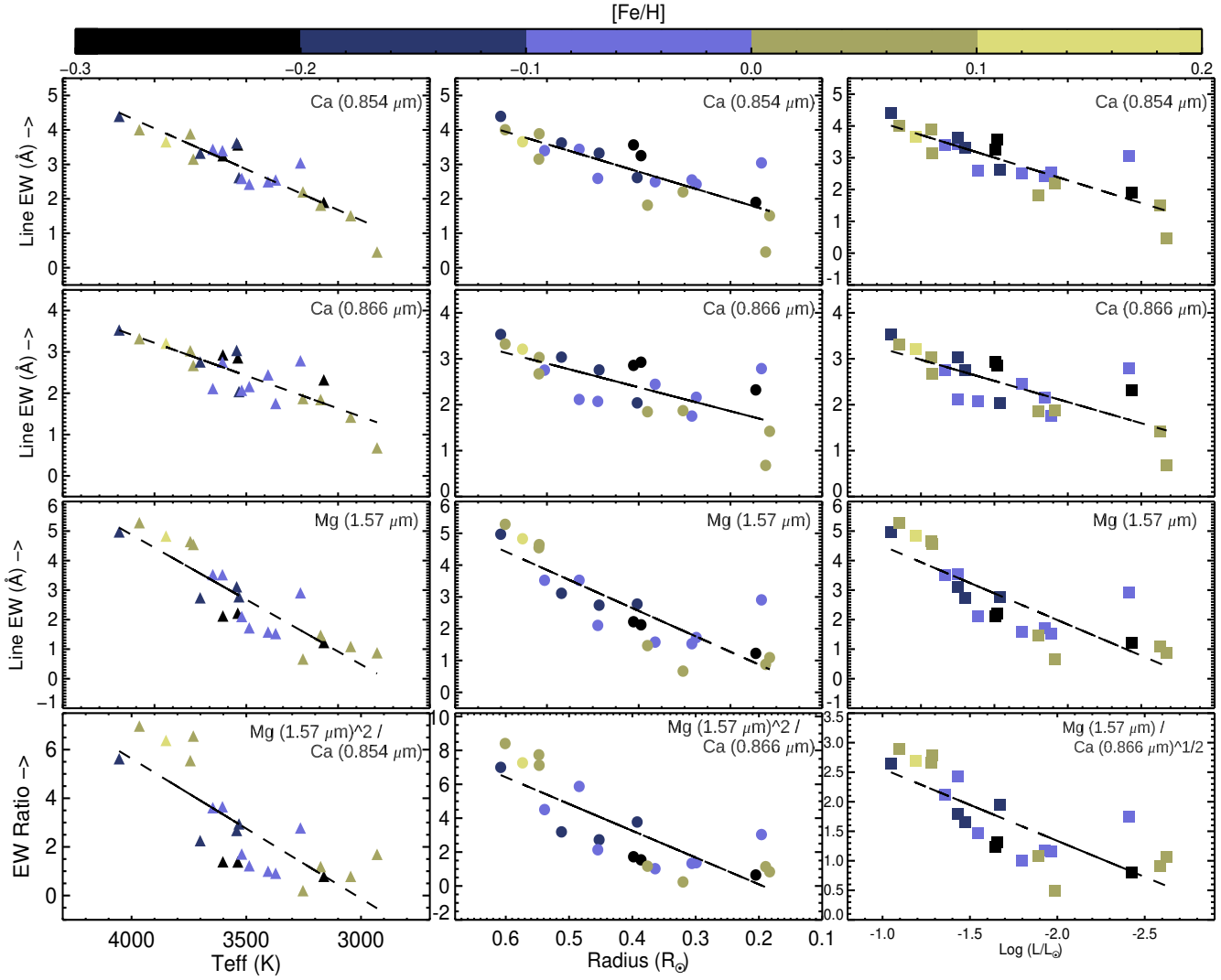


Figure 2. EWs and functional forms of EW ratios in optical and NIR CARMENES spectra that are used to establish best fitting calibration relationships are plotted against the measured T_{eff} , radius and luminosity ($\log L/L_{\odot}$) for our calibration sample. The data points are color-coded according to the $[\text{Fe}/\text{H}]$ values taken from Schweitzer et al. (2019) and the dashed straight lines represent the linear correlation.

Table 2. Measured EWs of the spectral features from the optical and NIR CARMENES spectra for the interferometric calibration sample.

Star	Ti (0.844 μm) (Å)	Ca (0.850 μm) (Å)	Ca (0.854 μm) (Å)	Ca (0.866 μm) (Å)	Mg (0.881 μm) (Å)	Ca (1.034 μm) (Å)	Na (1.140 μm) (Å)	K (1.169 μm) (Å)	K (1.243 μm) (Å)	K (1.252 μm) (Å)	Mg (1.574 μm) (Å)
GJ 172	1.231 ± 0.105	0.901 ± 0.007	4.393 ± 0.310	3.530 ± 0.202	0.756 ± 0.030	0.797 ± 0.022	2.019 ± 0.018	0.620 ± 0.015	0.066 ± 0.017	0.354 ± 0.011	4.971 ± 0.246
GJ 208	1.293 ± 0.055	0.803 ± 0.004	4.006 ± 0.145	3.320 ± 0.107	0.692 ± 0.017	—	2.340 ± 0.051	0.689 ± 0.008	0.188 ± 0.017	0.512 ± 0.008	5.283 ± 0.127
GJ 809	0.573 ± 0.038	0.796 ± 0.010	3.887 ± 0.187	3.028 ± 0.188	0.696 ± 0.025	0.817 ± 0.010	3.770 ± 0.009	0.986 ± 0.030	0.258 ± 0.005	0.451 ± 0.016	4.644 ± 0.126
GJ 412A	1.251 ± 0.026	0.752 ± 0.007	3.565 ± 0.147	2.856 ± 0.381	0.534 ± 0.019	0.786 ± 0.005	2.682 ± 0.021	0.733 ± 0.024	0.031 ± 0.013	0.302 ± 0.017	2.219 ± 0.106
GJ 15A	1.399 ± 0.090	0.760 ± 0.026	3.253 ± 0.430	2.926 ± 0.275	0.463 ± 0.025	0.822 ± 0.020	3.219 ± 0.018	0.866 ± 0.016	0.191 ± 0.021	0.375 ± 0.010	2.123 ± 0.218
GJ 649	1.283 ± 0.029	0.794 ± 0.009	3.399 ± 0.263	2.753 ± 0.211	0.335 ± 0.011	0.887 ± 0.017	3.646 ± 0.014	0.947 ± 0.025	0.245 ± 0.017	0.459 ± 0.006	3.523 ± 0.035
GJ 205	1.439 ± 0.052	0.867 ± 0.005	3.656 ± 0.174	3.209 ± 0.121	0.631 ± 0.016	—	4.125 ± 0.027	1.120 ± 0.027	0.310 ± 0.012	0.546 ± 0.015	4.829 ± 0.194
GJ 880	—	0.641 ± 0.010	3.153 ± 0.115	2.672 ± 0.273	0.143 ± 0.026	0.807 ± 0.021	4.489 ± 0.019	1.131 ± 0.028	0.288 ± 0.007	0.472 ± 0.010	4.547 ± 0.141
GJ 526	1.075 ± 0.042	0.761 ± 0.009	3.438 ± 0.266	2.114 ± 0.280	0.616 ± 0.015	0.773 ± 0.024	3.109 ± 0.038	0.776 ± 0.025	0.233 ± 0.008	0.396 ± 0.005	3.524 ± 0.090
GJ 411	0.007 ± 0.017	0.151 ± 0.007	2.616 ± 0.062	2.040 ± 0.144	0.064 ± 0.013	—	3.507 ± 0.010	0.502 ± 0.023	0.024 ± 0.008	0.063 ± 0.012	2.775 ± 0.027
GJ 176	1.315 ± 0.071	0.679 ± 0.009	3.325 ± 0.240	2.757 ± 0.141	0.617 ± 0.022	0.928 ± 0.028	2.152 ± 0.027	0.641 ± 0.029	0.011 ± 0.013	0.372 ± 0.010	2.740 ± 0.261
GJ 104	1.247 ± 0.180	0.777 ± 0.020	3.621 ± 0.455	3.036 ± 0.314	0.465 ± 0.049	0.900 ± 0.012	2.873 ± 0.025	0.577 ± 0.045	0.268 ± 0.018	0.528 ± 0.014	3.113 ± 0.099
GJ 436	1.006 ± 0.075	0.661 ± 0.012	2.593 ± 0.197	2.072 ± 0.578	0.500 ± 0.025	0.971 ± 0.012	3.220 ± 0.011	0.801 ± 0.012	0.269 ± 0.023	0.476 ± 0.009	2.104 ± 0.079
GJ 581	1.127 ± 0.062	0.560 ± 0.010	2.424 ± 0.461	2.162 ± 0.308	0.587 ± 0.017	0.996 ± 0.010	3.909 ± 0.016	1.208 ± 0.068	0.318 ± 0.014	0.539 ± 0.042	1.722 ± 0.293
GJ 109	1.389 ± 0.075	0.658 ± 0.015	2.495 ± 0.221	2.445 ± 0.224	0.449 ± 0.037	0.983 ± 0.011	4.051 ± 0.023	1.105 ± 0.019	0.276 ± 0.014	0.531 ± 0.008	1.579 ± 0.093
GJ 628	—	0.390 ± 0.011	2.548 ± 0.303	1.753 ± 0.182	0.135 ± 0.010	0.708 ± 0.031	3.457 ± 0.029	0.658 ± 0.069	0.281 ± 0.026	0.530 ± 0.018	1.528 ± 0.212
GJ 273	1.450 ± 0.065	0.531 ± 0.008	2.201 ± 0.263	1.871 ± 0.156	0.400 ± 0.020	0.011 ± 0.010	1.543 ± 0.013	0.124 ± 0.009	—	0.056 ± 0.014	0.666 ± 0.044
GJ 699	—	—	0.160 ± 0.290	0.642 ± 0.159	—	0.260 ± 0.018	2.087 ± 0.018	0.025 ± 0.034	—	0.014 ± 0.021	1.473 ± 0.085
GJ 729	1.652 ± 0.041	0.493 ± 0.012	1.898 ± 0.228	2.323 ± 0.200	0.467 ± 0.028	1.095 ± 0.042	4.497 ± 0.021	1.476 ± 0.015	0.498 ± 0.016	0.824 ± 0.015	1.225 ± 0.281
GJ 447	1.087 ± 0.101	0.700 ± 0.010	3.043 ± 0.252	2.786 ± 0.734	0.621 ± 0.033	0.880 ± 0.025	2.466 ± 0.020	0.588 ± 0.019	0.249 ± 0.009	0.463 ± 0.020	2.907 ± 0.346
GJ 876	1.410 ± 0.067	0.477 ± 0.022	1.815 ± 0.251	1.847 ± 0.532	0.444 ± 0.043	0.980 ± 0.031	4.513 ± 0.035	1.182 ± 0.053	0.418 ± 0.016	0.732 ± 0.017	1.469 ± 0.193
GJ 1253	—	0.066 ± 0.028	1.511 ± 0.781	1.421 ± 0.698	0.168 ± 0.110	0.627 ± 0.081	3.550 ± 0.025	0.409 ± 0.020	0.259 ± 0.017	0.847 ± 0.018	1.091 ± 0.263
GJ 905	—	—	0.456 ± 0.298	0.679 ± 0.807	0.135 ± 0.068	0.594 ± 0.056	4.048 ± 0.051	0.251 ± 0.083	—	0.366 ± 0.021	0.879 ± 0.103

Notes. Wavelengths are given in vacuum and the respective feature windows and continuums are given in Table 1.

Table 3. Linear Pearson Correlation Coefficient (LPCC) values between the features and stellar parameters for the calibration sample.

Feature	T_{eff} (K)	LPCC Radius (R_{\odot})	$\log(L/L_{\odot})$
Ti I (0.844 μm)	-0.17	-0.12	-0.17
Ca II (0.850 μm)	+0.70	+0.67	+0.69
Ca II (0.854 μm)	+0.87	+0.83	+0.86
Ca II (0.866 μm)	+0.81	+0.75	+0.78
Mg I (0.881 μm)	+0.55	+0.43	+0.46
Ca I (1.034 μm)	+0.28	+0.29	+0.31
Na I (1.140 μm)	-0.23	-0.06	-0.10
K I (1.169 μm)	+0.26	+0.30	+0.32
K I (1.243 μm)	-0.49	-0.32	-0.39
K I (1.252 μm)	-0.15	-0.04	-0.09
Mg I (1.574 μm)	+0.88	+0.85	+0.82

Notes : Wavelengths are given in vacuum.

Carlo simulation where multiple random realizations of Gaussian noise are added to the spectrum and EWs of the features are recalculated (Khata et al. 2020). The estimated EWs along with the associated errors of the spectral features from the optical and NIR CARMENES spectra for our interferometric calibration sample are given in Table 2.

3.2 Spectral features selection: Behavior with stellar parameters

We performed a principal component analysis (PCA) to search for the strongest correlations between the EWs of our calibration sample, and we calculated the linear Pearson correlation coefficients (LPCC) looking for legitimate correlation with the EWs and T_{eff} , radius, and luminosity. The LPCC value ranges from -1 to +1, and for two variables, such as X and Y, a positive correlation coefficient value indicates Y is increasing as X increases, and a negative value means Y decreases as X increases. We found that the EWs of Ca II (0.854 μm) and Ca II (0.866 μm) in the optical channel and the EWs of Mg I (1.574 μm) in the NIR channel attribute mostly in the first principal components (explaining 79% of the variance) in the PCA test. These three features also give the maximum LPCC values while we investigated for linear correlation with the stellar parameters, and we have given the respective LPCC values of the spectral features in Table 3. These two singly ionized Ca II (0.854 μm , 0.866 μm) lines (e.g., Ca II IRT infrared triplet) are prominent features in the spectra of cool M type stars and lie in a region of the spectrum with a well-defined continuum and are significantly free from telluric lines. Earlier work has helped to establish the sensitivity of these lines with stellar atmospheric parameters, such as Mallik (1994, 1997) and Andretta et al. (2005) tried to model the behavior of Ca II IRT line strength with T_{eff} , $\log g$ and metallicity; Zhou (1991) showed a significant effect of temperatures on Ca II IRT lines for cooler stars (up to M7) at low T_{eff} and Terrien et al. (2015) developed a technique to determine M-dwarfs M_k and radius using Ca II IRT feature. Among all the features in the optical and NIR band, Mg I (1.574 μm) shows the best correlation with the stellar parameters. The EW of the Mg I (1.574 μm) feature is used by Newton et al. (2015) to estimate the stellar radius of M dwarfs in the MEarth sample; Martinez et al. (2017) used this feature to calibrate T_{eff} and radius of K- and M-dwarf stars; and later the feature is also used by Khata et al. (2020) for the calibration of T_{eff} , radius and luminosity of low-resolution M-dwarfs spectra. Therefore, based on the PCA test and the best LPCC values obtained, we

selected these three spectral features from the initially considered 11 features for empirical calibrations of the stellar parameters.

In Fig. 2, we show the plot of the EWs and ratios of EWs for the selected spectral features [i.e., Ca (0.854 μm), Ca (0.866 μm), Mg (1.574 μm)] for the interferometric calibration sample against T_{eff} , radius and luminosity. The data points are color-coded by their respective metallicity ([Fe/H]) values as estimated by Schweitzer et al. (2019). As the atomic lines get broadened from early to later M dwarfs, the EWs decrease as effective temperature decreases. We see that the EWs of the two Ca II lines and the Mg I line and the line ratios behave almost in a linear fashion, implied by the dashed straight line fittings, as functions of T_{eff} , radius and $\log(L/L_{\odot})$ with no statistically significant metallicity dependence.

3.3 Empirical Calibrations of T_{eff} , radius and luminosity

While looking for the best-fit calibration relations, we found that simple linear functions of EWs or ratios of EW give better results than any higher order polynomial functions (e.g., Hoerl function [$ab^r * r^c$], power law [ar^b ; $b > 2$], exponential [ab^r], logarithmic [$a + b \ln(r)$; $r = \text{EW}$ or ratio of EW]). The same kind of linear fits are also observed in the work of Newton et al. (2015) but unlike them we did not restrict our fits to only the optical or NIR regions, rather we performed a comprehensive search by combining features from both bands simultaneously. For single-line EWs (we used lower case x, y, z as EWs: $x = \text{EW}_{\text{Ca}[0.854\mu\text{m}]}$; $y = \text{EW}_{\text{Ca}[0.866\mu\text{m}]}$; $z = \text{EW}_{\text{Mg}[1.574\mu\text{m}]}$), we tested with single component linear functions (e.g., $a + bX$; $a + bY$; $a + bZ$), where we used upper case X, Y, Z as simple functional forms of x, y, z (i.e., $X = x, x^2, x^{1/2}, 1/x, 1/x^2, 1/x^{1/2}$; $Y = y, y^2, y^{1/2}, 1/y, 1/y^2, 1/y^{1/2}$; $Z = z, z^2, z^{1/2}, 1/z, 1/z^2, 1/z^{1/2}$). We also did test single line double component functions (e.g., $a + bX + cX'$ [$X' \subseteq X$; $X' \neq X$]; $a + bY + cY'$ [$Y' \subseteq Y$; $Y' \neq Y$]; $a + bZ + cZ'$ [$Z' \subseteq Z$; $Z' \neq Z$]). We noticed that the use of more than two components in the linear relation did not give statistically better results, so we limited our test functions to a maximum of two components of EWs or ratio of EWs or combination of both. The multi-line functions (two components) that we tested are: $a + bX + cY$; $a + bX + cZ$; $a + bY + cZ$. The ratio of the spectral line depths or equivalent widths ($R = \text{EW}_1 / \text{EW}_2$) are found to be very sensitive temperature indicators (Kovtyukh et al. 2003) and tracers of other fundamental parameters with high efficiency and accuracy. So we also checked with all possible combinations of EW ratios of the three lines ($R_1 = X / Y$; $R_2 = X / Z$; $R_3 = Y / Z$). For single-ratio (one component) linear functions we did test: $a + R_i$ ($i = 1, 2, 3$), and single-line and single-ratio functions we tested: $a + bX + cR_i$; $a + bY + cR_i$; $a + bZ + cR_i$ ($i = 1, 2, 3$). Like the single-line double component functions, we tried out with single-ratio double component functions: $a + bR_i + cR'_i$ ($R'_i \subseteq R_i$; $R'_i \neq R_i$; $i = 1, 2, 3$) and also tested with multi-ratio functions: $a + bR_1 + cR_2$; $a + bR_1 + cR_3$; $a + bR_2 + cR_3$.

To find the best-fitting parameters from all possible combinations of linear functional relations, we performed multivariate linear regression and used the adjusted square of the multiple correlation coefficient (R_{ap}^2 , Rojas-Ayala et al. 2012), the root mean squared error (RMSE) and the mean absolute deviation (MAD) values to statistically compare the goodness of each fit. We show the calculations of RMSE, MAD and R_{ap}^2 as equation (A1), equation (A2) and equation (A3) in the appendix section. For a given set of calibration data, the R_{ap}^2 shows the proportion of variability in a data set that is accounted for by a regression model (an R_{ap}^2 value closer to 1 means a superior fit) and the RMSE (a lower RMSE means a better fit) evaluates the accuracy and predictive power of the response of the

Table 4. Different types of linear trial functions with one example each, using simple functional forms of the selected EWs and EW ratios ($x = \text{EW}_{Ca[0.854\mu\text{m}]}$; $y = \text{EW}_{Ca[0.866\mu\text{m}]}$; $z = \text{EW}_{Mg[1.574\mu\text{m}]}$) and associated RMSE, MAD and R^2_{ap} values of the stellar parameters. The upper case X, Y, Z represent functional forms of x, y, z (i.e., $X = x, x^2, x^{1/2}, 1/x, 1/x^2, 1/x^{1/2}; Y = y, y^2, y^{1/2}, 1/y, 1/y^2, 1/y^{1/2}; Z = z, z^2, z^{1/2}, 1/z, 1/z^2, 1/z^{1/2}$).

Nature of linear test functions	Example function	T_{eff} (K)			Radius (R_{\odot})			$\log(L/L_{\odot})$		
		RMSE	MAD	R^2_{ap}	RMSE	MAD	R^2_{ap}	RMSE	MAD	R^2_{ap}
single EW, single component [$a + bX$]	$a + bx$	147.15	111.90	0.737	0.082	0.062	0.672	0.253	0.174	0.730
single EW, single component [$a + bY$]	$a + by$	172.40	140.07	0.638	0.096	0.071	0.547	0.311	0.216	0.591
single EW, single component [$a + bZ$]	$a + bz$	137.18	108.68	0.771	0.076	0.055	0.712	0.282	0.216	0.663
single EW, double component [$a + bX + cX'$ ($X' \subseteq X; X' \neq X$)]	$a + bx + cx^2$	126.75	98.00	0.805	0.078	0.053	0.701	0.249	0.171	0.737
single EW, double component [$a + bY + cY'$ ($Y' \subseteq Y; Y' \neq Y$)]	$a + by + cy^2$	166.72	132.76	0.662	0.097	0.066	0.540	0.318	0.215	0.573
single EW, double component [$a + bZ + cZ'$ ($Z' \subseteq Z; Z' \neq Z$)]	$a + bz + cz^2$	138.66	109.38	0.766	0.078	0.053	0.699	0.283	0.195	0.661
double EWs, double component [$a + bX + cY$]	$a + bx + cy$	150.66	112.24	0.724	0.083	0.062	0.663	0.254	0.175	0.726
double EWs, double component [$a + bX + cZ$]	$a + bx + cz$	114.20	85.69	0.841	0.069	0.041	0.769	0.230	0.139	0.777
double EWs, double component [$a + bY + cZ$]	$a + by + cz$	124.14	98.57	0.812	0.074	0.046	0.730	0.261	0.172	0.712
single EW ratio, single component [$a + bR_1$ ($R_1 = X/Y$)]	$a + bx/y$	248.36	191.47	0.250	0.119	0.095	0.299	0.390	0.309	0.357
single EW ratio, single component [$a + bR_2$ ($R_2 = X/Z$)]	$a + bx/z$	285.48	209.99	0.008	0.143	0.112	-0.008	0.493	0.383	-0.029
single EW ratio, single component [$a + bR_3$ ($R_3 = Y/Z$)]	$a + by/z$	264.92	193.59	0.146	0.134	0.106	0.115	0.466	0.362	0.081
single EW & single EW ratio, double component [$a + bX + cR_1$]	$a + bx + cx/y$	140.03	110.91	0.761	0.083	0.060	0.662	0.258	0.171	0.719
single EW & single EW ratio, double component [$a + bX + cR_2$]	$a + bx + cx/z$	128.86	100.45	0.798	0.077	0.052	0.710	0.246	0.159	0.745
single EW & single EW ratio, double component [$a + bX + cR_3$]	$a + bx + cy/z$	128.28	101.01	0.800	0.076	0.053	0.715	0.241	0.156	0.753
single EW & single EW ratio, double component [$a + bY + cR_1$]	$a + by + cx/y$	173.69	133.40	0.633	0.094	0.072	0.566	0.296	0.208	0.629
single EW & single EW ratio, double component [$a + bY + cR_2$]	$a + by + cx/z$	159.53	124.71	0.690	0.093	0.064	0.574	0.309	0.204	0.596
single EW & single EW ratio, double component [$a + bY + cR_3$]	$a + by + cy/z$	143.75	109.19	0.749	0.087	0.057	0.631	0.288	0.185	0.648
single EW & single EW ratio, double component [$a + bZ + cR_1$]	$a + bz + cx/y$	130.58	101.53	0.793	0.070	0.048	0.758	0.245	0.174	0.745
single EW & single EW ratio, double component [$a + bZ + cR_2$]	$a + bz + cx/z$	124.47	98.52	0.811	0.070	0.044	0.762	0.246	0.172	0.744
single EW & single EW ratio, double component [$a + bZ + cR_3$]	$a + bz + cy/z$	132.00	105.23	0.788	0.074	0.049	0.733	0.268	0.197	0.697
single EW ratio, double component [$a + bR_1 + cR'_1$ ($R'_1 \neq R_1$)]	$a + bx/y + cx/y^2$	181.69	138.02	0.598	0.100	0.078	0.507	0.305	0.222	0.605
single EW ratio, double component [$a + bR_2 + cR'_2$ ($R'_2 \neq R_2$)]	$a + bx/z + cx/z^2$	261.95	196.47	0.165	0.136	0.111	0.082	0.453	0.362	0.131
single EW ratio, double component [$a + bR_3 + cR'_3$ ($R'_3 \neq R_3$)]	$a + by/z + cy/z^2$	262.06	189.85	0.164	0.136	0.104	0.093	0.464	0.352	0.088
double EW ratio, double component [$a + bR_1 + cR_2$]	$a + bx/y + cx/z$	222.67	168.38	0.397	0.108	0.085	0.426	0.361	0.282	0.447
double EW ratio, double component [$a + bR_1 + cR_3$]	$a + bx/y + cy/z$	220.25	165.42	0.410	0.108	0.084	0.429	0.359	0.274	0.455
double EW ratio, double component [$a + bR_2 + cR_3$]	$a + bx/z + cy/z$	229.74	171.63	0.358	0.116	0.093	0.335	0.385	0.299	0.372
Accepted linear functions for T_{eff} (★), Radius (†) and Luminosity (§) respectively with minimum RMSE and maximum R^2_{ap} values										
(★) single EW & single EW ratio, double component	$a + bx + cz^2/x$	99.00	70.97	0.881						
(†) single EW & single EW ratio, double component	$a + bx + cz^2/y$				0.067	0.043	0.779			
(§) double EW ratio, double component	$a + bz/\sqrt{y} + cx/\sqrt{z}$							0.218	0.137	0.798

Notes. Table 4 is available in its entirety in the electronic version of the journal as supplementary material.

regression model (Khata et al. 2020). We tested 8001 possible combinations of linear trial functions using the selected EWs and EW ratios and in Table 4 we show different types of linear trial functions with one example each, alongwith the respective RMSE, MAD and R^2_{ap} values for T_{eff} , radius and luminosity. In the case of RMSE, the individual errors are squared and the RMSE gives relatively high weight to large errors, whereas for MAD the errors are co-added in a linear fashion attributing equal weightage on small and large errors. This means the RMSE is more suitable when large deviation from the mean is particularly undesirable. Also as our estimated errors on the EWs are expected to be Gaussian in nature, the RMSE is more appropriate to represent a model performance than the MAD. So we selected the best fitting calibration relations for the stellar parameters mainly on the basis of highest R^2_{ap} and lowest RMSE values. To get a clear understanding of how much better the chosen relations are than the rest of the trial functions, we show a representation of the RMSE, MAD and R^2_{ap} values in Fig. 3. We find that for T_{eff} , our chosen function also gives the lowest MAD value alongside the lowest RMSE value, but for the best fitting radius ($MAD_{rad} = 0.043$) and luminosity ($MAD_{lum} = 0.137$) relations the MAD values are slightly greater than the lowest estimated values ($MAD_{lowest,rad} = 0.040$ and $MAD_{lowest,lum} = 0.124$). The selected calibration relations for the stellar parameters are given as :

$$T_{\text{eff}}/K = A + B \times Ca(0.854\mu\text{m}) + C \times \frac{[Mg(1.57\mu\text{m})]^2}{Ca(0.854\mu\text{m})} \quad (2)$$

$$A = 2738.37 \pm 39.5 ; B = 232.046 \pm 7.6 ; C = 35.462 \pm 2.6$$

$$R^2_{ap} = 0.881 ; \quad \text{RMSE } (T_{\text{eff}}/\text{K}) = 99.0 ; \quad \text{MAD } / K = 71.0$$

$$R/R_{\odot} = A + B \times Ca(0.854\mu\text{m}) + C \times \frac{[Mg(1.57\mu\text{m})]^2}{Ca(0.866\mu\text{m})} \quad (3)$$

$$A = 0.1102 \pm 0.01 ; B = 0.0757 \pm 0.002 ; C = 0.0231 \pm 0.0009$$

$$R^2_{ap} = 0.779 ; \quad \text{RMSE } (R/R_{\odot}) = 0.067 ; \quad \text{MAD } / R_{\odot} = 0.043$$

$$\log L/L_{\odot} = A + B \times \frac{Ca(0.854\mu\text{m})}{[Mg(1.57\mu\text{m})]^{1/2}} + C \times \frac{Mg(1.57\mu\text{m})}{[Ca(0.866\mu\text{m})]^{1/2}} \quad (4)$$

$$A = -3.5063 \pm 0.032 ; B = 0.4896 \pm 0.004 ; C = 0.5363 \pm 0.003$$

$$R^2_{ap} = 0.798 ; \quad \text{RMSE } (\log L/L_{\odot}) = 0.218 ; \quad \text{MAD } / \text{dex} = 0.137$$

We show the plots of our best-fitting linear relationships and the respective residuals of the parameters for the calibrator stars in Fig. 4. The final errors on the stellar parameters are estimated by combining the randomly generated Gaussian error propagated from the EWs of the features with the intrinsic scatter (RMSE) inherent in the calibration relations. In Table 5, we present the inferred stellar parameters with associated errors that we estimated using the calibration relations. For our work, we notice that along with the

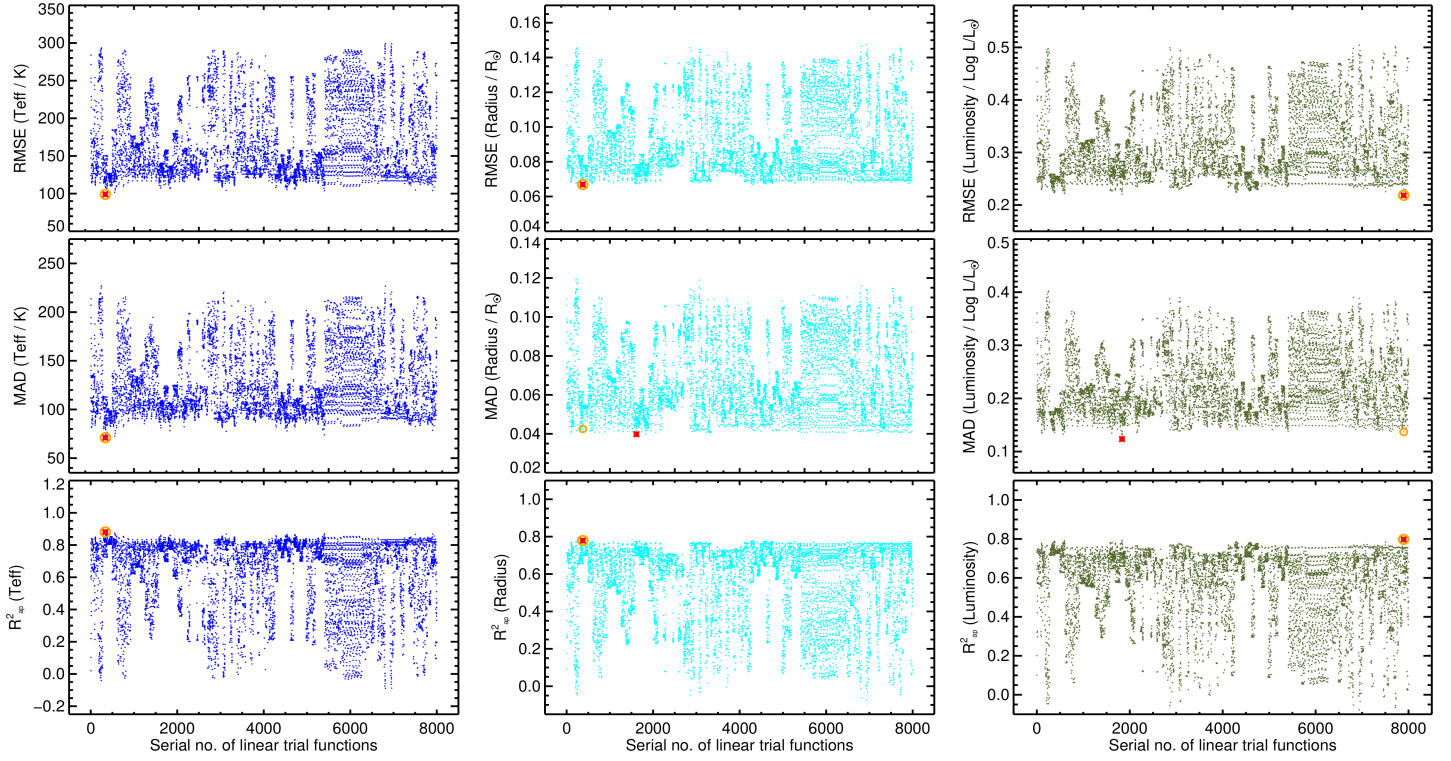


Figure 3. A representation of the estimated RMSE, MAD and R^2_{ap} (plotted along the y-axes) of the different trial functions (plotted along the x-axes going from 1 to 8001) for T_{eff} (left panel, blue color), radius (middle panel, cyan color) and log luminosity (right panel, olive color) is shown here. The respective RMSE, MAD and R^2_{ap} values of the chosen best fitting functions are marked by orange circles and the lowest values of RMSE and MAD and the highest value of R^2_{ap} are represented by the red star symbols.

Table 5. Inferred T_{eff} , radius and L_{bol} for the calibration sample.

Star	Teff (K)		Radius (R_{\odot})		$\log L/L_{\odot}$	
	Measured	Inferred ^(e)	Measured	Inferred ^(f)	Measured	Inferred ^(g)
Gl 172 ^a	4054±38	3957±108	0.608±0.020	0.604±0.067	-1.048±0.009	-1.12±0.23
Gl 208 ^a	3966±60	3915±106	0.601±0.020	0.608±0.068	-1.097±0.010	-1.10±0.23
GJ 809 ^b	3744±27	3837±111	0.547±0.006	0.569±0.067	-1.280±0.005	-1.19±0.22
GJ 412A ^b	3537±41	3615±107	0.398±0.009	0.420±0.067	-1.655±0.004	-1.63±0.22
GJ 15A ^b	3602±13	3542±104	0.386±0.002	0.392±0.066	-1.647±0.005	-1.75±0.22
GJ 649 ^d	3604±46	3657±107	0.539±0.015	0.472±0.067	-1.359±0.002	-1.48±0.22
GJ 205 ^b	3850±22	3813±105	0.574±0.004	0.555±0.067	-1.190±0.009	-1.25±0.22
GJ 880 ^b	3731±16	3703±112	0.548±0.004	0.528±0.068	-1.286±0.004	-1.29±0.23
GJ 526 ^b	3646±34	3664±105	0.484±0.008	0.506±0.067	-1.433±0.006	-1.31±0.22
GJ 411 ^b	3532±17	3450±103	0.392±0.003	0.395±0.066	-1.671±0.006	-1.70±0.22
GJ 176 ^d	3701±90	3590±106	0.453±0.022	0.425±0.067	-1.475±0.003	-1.64±0.22
Gl 104 ^a	3542±62	3674±112	0.512±0.022	0.458±0.069	-1.432±0.012	-1.54±0.23
GJ 436 ^b	3520±66	3401±118	0.455±0.018	0.356±0.068	-1.548±0.011	-1.85±0.23
GJ 581 ^b	3487±62	3344±108	0.299±0.010	0.325±0.067	-1.928±0.007	-1.97±0.22
Gl 109 ^a	3405±60	3353±110	0.364±0.014	0.323±0.067	-1.797±0.015	-1.99±0.23
GJ 628 ^c	3372±12	3362±104	0.306±0.007	0.334±0.066	-1.965±0.070	-1.88±0.22
GJ 273 ^c	3253±39	3256±113	0.320±0.005	0.282±0.068	-1.988±0.102	-1.92±0.23
GJ 699 ^b	3238±11	3256±111	0.187±0.001	0.200±0.066	-2.466±0.003	-2.46±0.22
GJ 729 ^c	3162±30	3207±107	0.205±0.006	0.269±0.067	-2.424±0.169	-2.24±0.22
GJ 447 ^c	3264±24	3543±109	0.196±0.010	0.411±0.067	-2.408±0.198	-1.70±0.23
GJ 876 ^d	3176±20	3202±107	0.376±0.005	0.275±0.067	-1.889±0.002	-2.19±0.23
Gl 1253 ^a	3045±60	3117±107	0.183±0.009	0.244±0.067	-2.588±0.047	-2.31±0.23
Gl 905 ^a	2930±60	2904±125	0.189±0.007	0.171±0.069	-2.626±0.041	-2.70±0.23

Notes. Interferometrically measured parameters are taken from ^a Mann et al. (2015); ^b Newton et al. (2015); ^c Markus Rabus et al. (2019); ^d Mann et al. (2013b). ^(e) T_{eff} is inferred using equation (2), the fitting is shown in Fig. 4, top left panel; ^(f) Radius is inferred using equation (3), the fitting is shown in Fig. 4, top right panel; ^(g) $\log L/L_{\odot}$ is inferred using equation (4), the fitting is shown in Fig. 4, bottom panel.

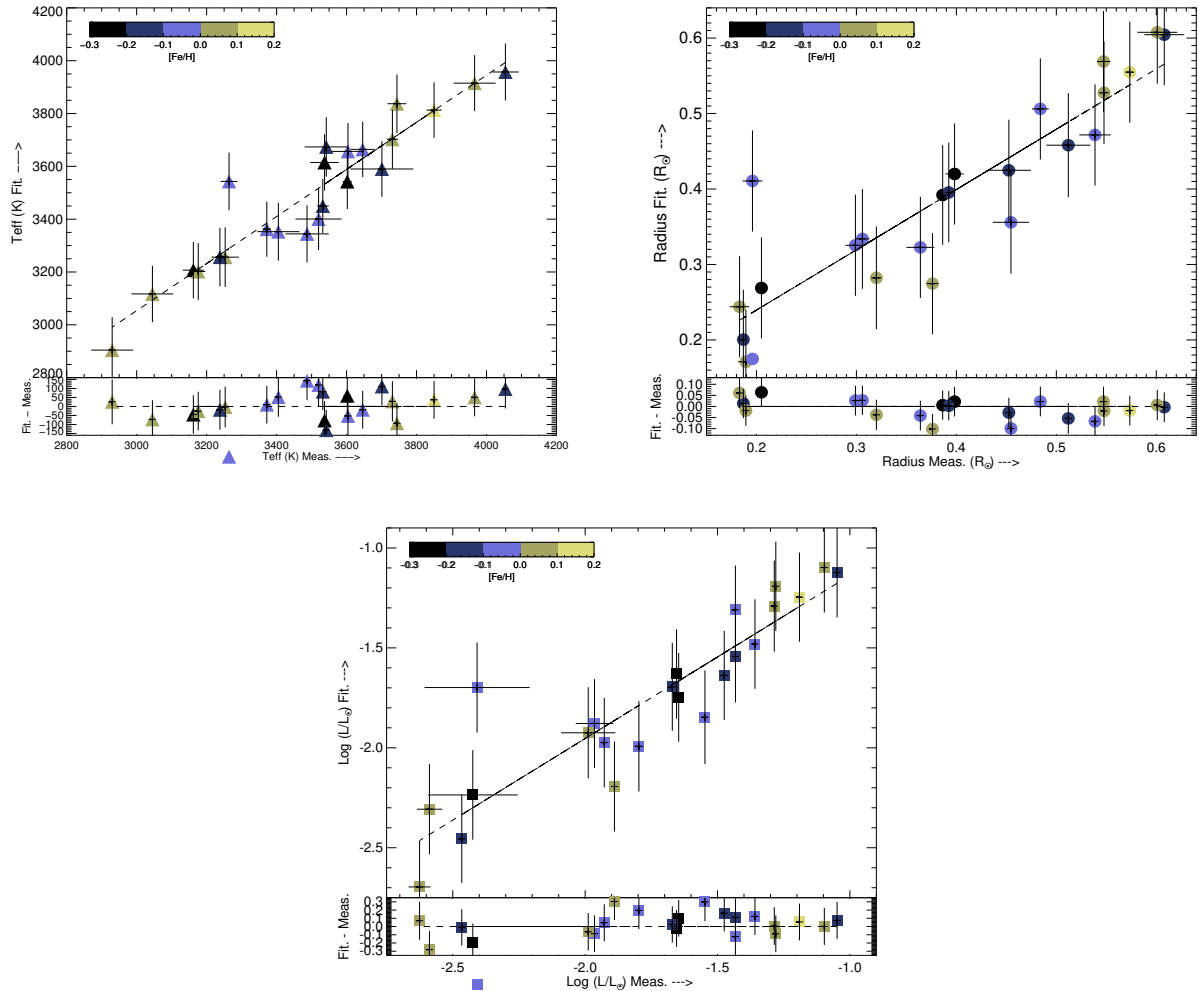


Figure 4. We show the plots of our best-fitting calibration relationships and the respective residuals for T_{eff} (filled triangles in the top left panel), radius (filled circles in the top right panel), and $\log(L/L_{\odot})$ (filled squares in bottom panel) here. The horizontal axes show the directly measured stellar parameters taken from Boyajian et al. (2012), Mann et al. (2013b, 2015) and Markus Rabus et al. (2019). In the top plot of each panel, the vertical axes represent the stellar parameters inferred from the best fits of this work; and in the lower plot of each panel, the vertical axes represent the residuals between the best-fitting values and the measured values. The data points are color-coded by the $[\text{Fe}/\text{H}]$ values from Schweitzer et al. (2019).

EWs, the simple functional form of the ratios of EWs plays an important role in the calibration. In principle, the change in EWs with T_{eff} for lines with higher excitation potential (χ) should be faster than that for lines with lower ' χ ' and a ratio of EWs should be temperature sensitive if the excitation potential of the lines differs by as much as possible (Gray 1994). The excitation potential of the Ca II IRT lines are 1.70 eV and 1.69 eV, respectively, and for the Mg I triplet, the ' χ ' value is around 5.93 eV, so the EW ratios $Mg(1.57\mu\text{m})/Ca(0.854\mu\text{m})$ and $Mg(1.57\mu\text{m})/Ca(0.866\mu\text{m})$ show better correlation with the stellar parameters than the ratio of the two Ca II IRT lines [i.e., $Ca(0.854\mu\text{m})/Ca(0.866\mu\text{m})$]. Also as the EWs show very negligible metallicity dependence within the parameter-space, selecting the lines from different part of the spectra does not hamper the calibration substantially.

In Fig. 5, we show the T_{eff} -radius (left panel) and T_{eff} -luminosity (right panel) distribution of our sample of the CARMENES M-dwarfs. For comparison, in the left panel, we overplot the radius-temperature relation from Mann et al. (2015, hereafter Mann15) and new evolutionary models of ages 0.2 Gyr, 2.0 Gyr, and 10.0 Gyr for pre-main sequence and main sequence low-mass stars down to the hydrogen-burning limit for solar metallicity by Baraffe et al.

(2015, hereafter BHAC15). Our estimated radii are a little larger than what is predicted by Mann15's relation and have a distinct separation from the BHAC15 isochrones. One reason for the disagreement could be that the stellar radii for low-mass stars generally are measured to be larger than model predictions (Boyajian et al. 2012). Another reason could be the metallicity dependence of parameters (Newton et al. 2015) which is observed in our temperature-radius plane. It can be seen that for $T_{\text{eff}} < 3700$, a large part of our sample is metal poor. In the right panel of Fig. 5, we also show the overplot of the BHAC15 isochrones and the 5 Gyr, Dartmouth isochrones (Dotter et al. 2008; Feiden et al. 2011) for super-solar ($[\text{Fe}/\text{H}] = +0.30$ dex), solar ($[\text{Fe}/\text{H}] = 0.0$ dex) and sub-solar ($[\text{Fe}/\text{H}] = -0.50$ dex) metallicity. Here also metallicity has a significant effect on the models (as noted by Newton et al. 2015), and the Dartmouth models predict that for cool stars, there will be a difference of 1 in absolute magnitude for a star with $[\text{Fe}/\text{H}] = -0.50$ dex, compared to another star of same effective temperature with $[\text{Fe}/\text{H}] = +0.30$ dex.

In Table B1, we present the estimated EWs of the selected spectral features that we use for the calibration and the stellar parameters of the CARMENES M-dwarf stars. We also show a plot

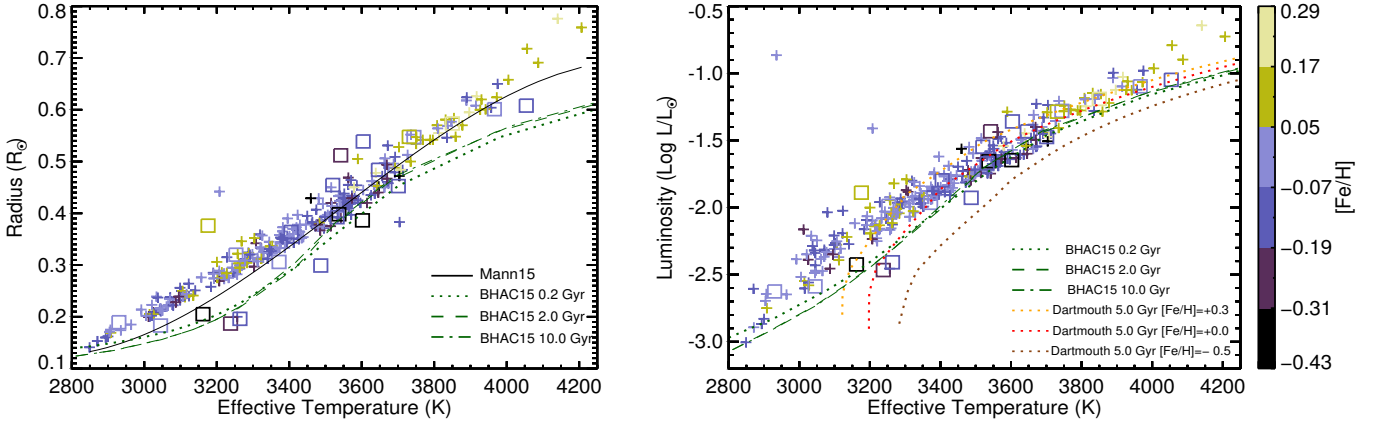


Figure 5. Stellar radius vs. effective temperature (left panel) and luminosity vs. effective temperature (right panel) plot, showing parameter values of CARMENES M-dwarfs (plus symbols) estimated using EW dependent calibration relations and measured values of interferometric calibrators (open square symbols). For the radius vs T_{eff} plot, we overplot the best-fit radius-temperature relation (solid black line) from Mann15 (Mann et al. 2015) and 0.2 Gyr, 2.0 Gyr and 10.0 Gyr isochrones (represented by green dotted, dashed and dash-dot lines respectively) for $[\text{Fe}/\text{H}] = 0.0$ and $\log g \approx 5.0$ from BHAC15 (Baraffe et al. 2015). For the luminosity- T_{eff} plot, we also show the isochrones from BHAC15 along with the 5 Gyr Dartmouth isochrones for $[\text{Fe}/\text{H}] = 0.3$ (dotted orange line), $[\text{Fe}/\text{H}] = 0.0$ (dotted red line) and $[\text{Fe}/\text{H}] = -0.5$ (dotted brown line). The data points are color-coded by metallicity from Schweitzer et al. (2019).

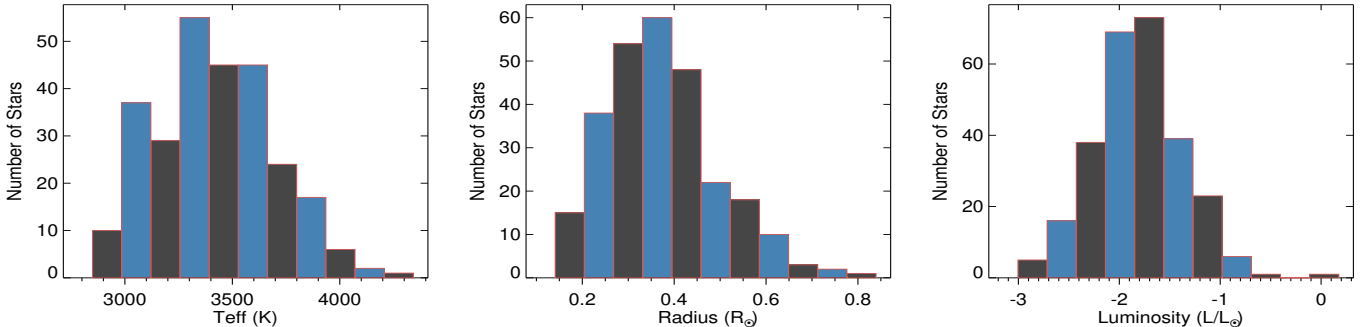


Figure 6. The distribution of estimated T_{eff} ($2849 < T_{\text{eff}}(\text{K}) < 4206$), radius ($0.141 < R/R_{\odot} < 0.776$) and luminosity ($-3.00 < \log L/L_{\odot} < -0.643$) of the CARMENES M-dwarfs are shown here.

of the distribution of the stellar parameters of our M-dwarf sample in Fig. 6 with the parameter values ranging T_{eff} ($2849 < T_{\text{eff}}(\text{K}) < 4206$), radius ($0.141 < R/R_{\odot} < 0.776$) and luminosity ($-3.00 < \log L/L_{\odot} < -0.643$).

3.4 Comparison with literature studies

In Fig. 7, we show the comparison of the results that we get in this work (horizontal axes) with the literature parameter values obtained in other works (vertical axes) using different techniques for the overlapping M-dwarfs. In Table 6, we present the median and standard deviation of the differences between the various literature values and the values determined here. For better readability, we do not use error bars in the plots; rather, we show median errors of all the comparisons in the lower right side of each plot.

In the top panel of Fig. 7, we compare our estimated T_{eff} with different literature works. Passegger et al. (2020, hereafter Passegger20) derived T_{eff} using neural network architecture for CARMENES spectra, Mann15 calculated T_{eff} by comparing their optical spectra with BT-Settl (PHOENIX) models, Maldonado et al. (2015, hereafter Maldonado15) used ratios of pseudo EWs of spectral features as temperature diagnostic and Houdebine et al. (2019, hereafter Houdebine19) used a photometric approach and

correlated $(R - I)_C$ color with T_{eff} . Apart from some minor scatter, all these results show reasonably good median and standard deviation values of differences with our estimation and overlap (within their error) of the dotted line region which represents $\pm 110\text{K}$ from a one-to-one comparison. Comparing the CARMENES spectra with the BT-Settl models both in the optical and in the NIR simultaneously, Rajpurohit et al. (2018, hereafter Rajpurohit18) estimated T_{eff} with a median error around 100K and Schweitzer et al. (2019, hereafter Schweitzer19) measured the T_{eff} by fitting the CARMENES spectra of the visual (VIS) channel with PHOENIX-ACES synthetic spectra (Husser et al. 2013). Rajpurohit18 and Schweitzer19 show relatively consistent results as the data points stay well within the dotted line region down to 3500K . Below 3500K some of the estimated T_{eff} values (from Rajpurohit18 and Schweitzer19) are up to 300K higher than our values. Although for both the cases, the overall median and standard deviation in differences are less than 90K .

The comparison of the radius is shown in the middle panel of Fig. 7. Newton et al. (2017, hereafter Newton17) and Mann15 empirically calibrated stellar radius, Maldonado15 used photometric estimates of radius to calibrate empirical relations using temperatures and metallicities, and Houdebine19 used V-band absolute magnitude and T_{eff} to determine the radii. We observe that the radii

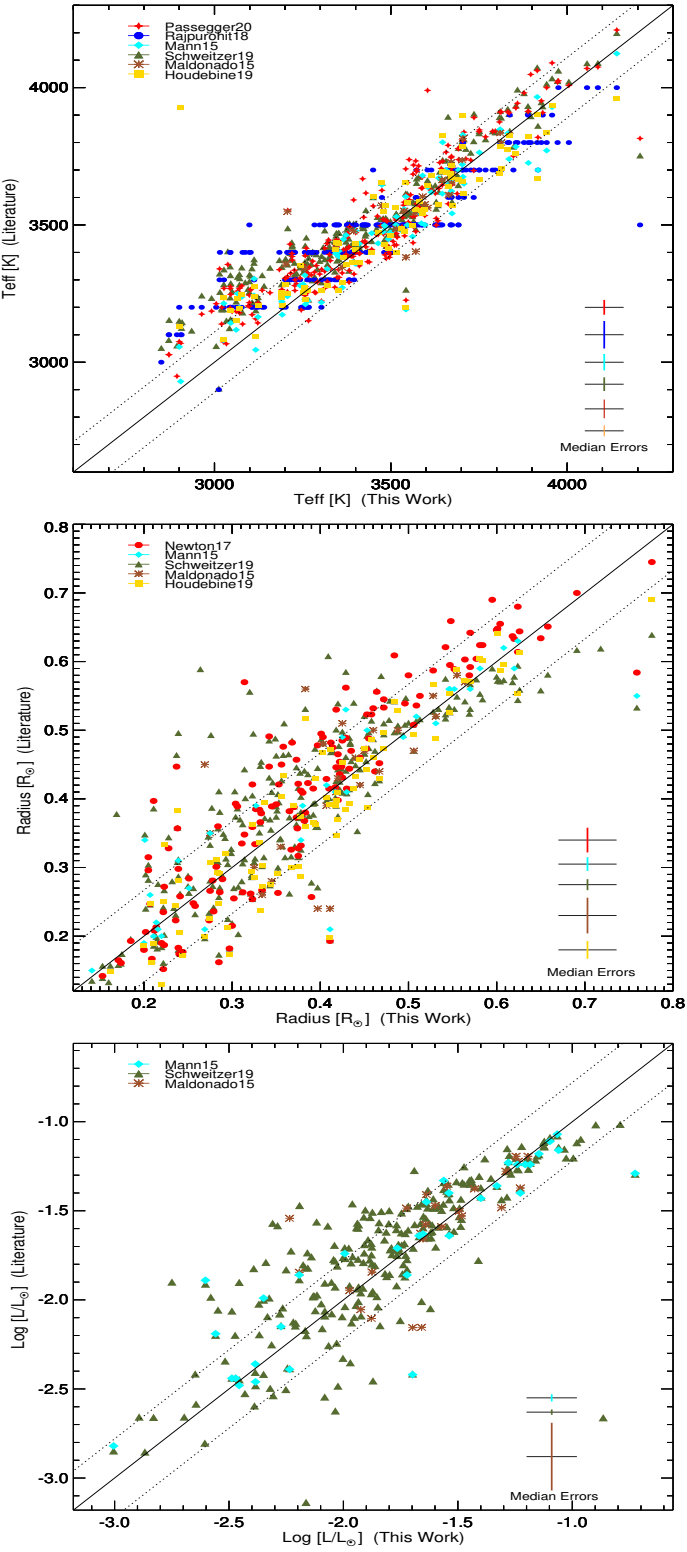


Figure 7. Comparisons of T_{eff} (top panel), radius (middle panel) and luminosity (bottom panel) with literature results (vertical axes) and this work (horizontal axes). The 1:1 relation is indicated by the solid black lines and the dotted lines indicate the typical size of the error bars associated with our work. The median errors associated with the literature values are shown in the lower right corner of each plot. Different determination methods of literature values are indicated by different symbols and colors. Legends used in the plots : Passegger20 (Passegger et al. 2020); Rajpurohit18 (Rajpurohit et al. 2018); Mann15 (Mann et al. 2015); Schweitzer19 (Schweitzer et al. 2019); Maldonado15 (Maldonado et al. 2015); Houdebine19 (Houdebine et al. 2019); Newton17 (Newton et al. 2017).

Table 6. Median and standard deviation (Std. Dev.) of differences between the results of literature and this work for stellar parameters

Literature	T_{eff} (K)	Radius (R_{\odot})	$\log(L/L_{\odot})$
Schweitzer et al. (2019)	75 / 80	0.038 / 0.050	0.13 / 0.22
Maldonado et al. (2015)	33 / 75	0.025 / 0.056	0.064 / 0.179
Mann et al. (2015)	45 / 60	0.019 / 0.052	0.10 / 0.19
Houdebine et al. (2019)	58 / 63	0.012 / 0.055	–
Passegger et al. (2020)	73 / 69	–	–
Rajpurohit et al. (2018)	83 / 86	–	–
Newton et al. (2017)	–	0.043 / 0.045	–

estimated by Newton17 and Houdebine19 are larger than our values down to $0.3R_{\odot}$ and for radii smaller than that, their values are slightly lower than ours. Schweitzer19 has the biggest scatter (compared to our results), with radii that are generally slightly larger than ours. These discrepancies might be related to the activity level of M-dwarfs (Morales, Ribas and Jordi 2008) as either strong magnetic fields predictably inhibiting convection or flux conservation in a magnetic spot-covered stellar surface (López-Morales & Ribas 2005) causes larger radii for a given T_{eff} . Also, Schweitzer19 used effective temperature to calculate the radii using Stefan-Boltzmann's law while they derived their T_{eff} by fitting with synthetic spectra, and experimental evidence suggests that theoretical models have limitations to describe star's T_{eff} accurately for a value lower than 4000K and that could add errors in radii. However, despite the scatter, the literature radii show consistency with our estimations with the median and standard deviation of differences being well below the median value of our radius uncertainty ($0.067 R_{\odot}$).

In the bottom panel of Fig. 7, we show the luminosity comparison for three literature results: Mann15 estimated luminosity using empirical relations, using apparent magnitudes and distances, Schweitzer19 photometrically determined luminosity, and Maldonado15 used the Stefan-Boltzmann law. In general Schweitzer19 is in good agreement with the one-to-one relationship, however there is some scatter in the luminosity ($\log L/L_{\odot}$) in the range of -1.5 to -2.0 dex. This mismatch could arise from the discrepancy in the value of the apparent magnitudes as experimental evidence suggests that active and inactive M dwarfs define different sequences in the luminosity-color plane (Stauffer & Hartmann 1986) plane and the uncertainty of distance calculation adds to the inconsistency.

4 SUMMARY AND CONCLUSION

We have estimated effective temperature, radius, and luminosity (L/L_{\odot}) with individual error bars for a sample of 271 M-dwarf stars with spectral types (M0V–M7V) observed in the CARMENES radial-velocity planet survey. We establish new empirical calibration relationships to determine fundamental parameters of low mass M-dwarf stars using EWs and EW ratios of spectral absorption features taken simultaneously from high resolution ($R \sim 90000$) optical (0.52 – $0.96 \mu\text{m}$) and near-infrared (0.96 – $1.71 \mu\text{m}$) spectra. The estimation of our physical properties is mostly model-independent, and the main results are summarized as follow:

- (1) The optical and NIR spectra of CARMENES M-dwarfs contain several important spectral absorption features, which show a legitimate strong correlation with the physical parameters. We select a sample of 23 stars with interferometrically measured radii as our calibrators. We perform principal component analysis (PCA),

looking for the strongest correlations among the measured EWs of our calibration sample and derive the linear Pearson correlation coefficient to identify the most suitable tracers of the stellar parameters.

(2) The optical (Ca II at $0.854 \mu\text{m}$, Ca II at $0.866 \mu\text{m}$) and NIR (Mg I at $1.574 \mu\text{m}$) features show a strong correlation with the stellar parameters giving the best correlation coefficient values. We find that the absorption lines of low and high excitation potentials (χ) respond differently to the change of stellar parameters and the inclusion of the ratio of the equivalent widths with different excitation potentials in the calibration relations gives comparatively superior results.

(3) We investigate simple parameterizations of two EWs or EW ratios or a combination of both and examine every possible single line or multiline linear function. We have performed multivariate linear regression to determine the best fitting parameters and use the adjusted square of the multiple correlation coefficient (R_{ap}^2), the RMSE, and the mean absolute deviation (MAD) values to statistically compare the goodness of each fit.

(4) We notice that the simultaneous use of the EWs and ratios of EWs of these selected features from both the optical and NIR band give the best fit linear calibration relationships of T_{eff} , radius, and luminosity with the RMSE values of 99K , $0.06R_{\odot}$ and 0.22dex respectively. Our parameter values cover ranges in the parameter-space of ($2849 < T_{\text{eff}}(\text{K}) < 4206$), ($0.141 < R/R_{\odot} < 0.776$) and ($-3.00 < \log L/L_{\odot} < -0.643$). The radii and luminosities derived in this work are found to be larger than what is predicted by the theoretical evolutionary models and show some metallicity dependence as we see for $T_{\text{eff}} < 3700 \text{ K}$, where our sample is mostly metal poor.

(5) We also explore and compare our results with literature values obtained with other methods where available. Though the comparison plots display little differences in terms of the median and standard deviation values, the overall agreement is good. Our calibrations can be very useful for understanding the properties of potential planet-host candidates and distant cool stars without parallaxes and flux calibrated spectra.

5 ACKNOWLEDGEMENTS

The authors are grateful to the reviewer for all the valuable comments and suggestions, which helped to improve the overall quality of this paper. The work is supported by S. N. Bose National Centre for Basic Sciences under the Department of Science and Technology (DST), Govt. of India. The research work leading to this publication has received funding from the INSPIRE Fellowship scheme by the DST, Govt. of India. The result of this research is "Based on data from the CARMENES data archive at CAB (INTA-CSIC)." The authors acknowledge the use of the SIMBAD and VizieR database, operated at CDS, Strasbourg, France. This research made use of the IDL-based tellrv and nirew packages developed by E. R. Newton.

6 DATA AVAILABILITY

All the observational data that we have used for the research work of this paper are publicly available in the CARMENES data archive at CAB (INTA-CSIC) (<http://carmenes.cab.inta-csic.es/gto/jsp/reinersetal2018.jsp>). Table 4 is available in its entirety as online supplementary material in the journal.

REFERENCES

- Allard, F., Homeier, D., & Freytag, B. 2012, *Philosophical Transactions of the Royal Society of London Series A*, **370**, 2765
 Allard, F., Homeier, D., Freytag, B., et al. 2013, *Memorie della Societa Astronomica Italiana Supplementi*, **24**, 128
 Alonso-Floriano, F. J., Morales, J. C., Caballero, J. A., et al. 2015, *A&A*, **577**, A128
 Andretta, V., Busá, I., Gomez, M. T., & Terranegra, L., 2005, *A&A*, **430**, 669
 Anglada-Escudé, G., Amado, P. J., Barnes, J., et al. 2016, *Nature*, **536**, 437
 Antoniadis-Karnavas, A., Sousa, S. G., Delgado-Mena, E., et al. 2020, *A&A*, **636**, A9
 Ballard, S., Charbonneau, D., Fressin, F., et al. 2013, *ApJ*, **773**, 98
 Baraffe, I., Homeier, D., Allard, F., & Chabrier, G. 2015, *A&A*, **577**, A42
 Berger, D. H., Gies, D. R., McAlister, H. A., et al. 2006, *ApJ*, **644**, 475
 Bessell, M.S. 1991, *AJ*, **101**, 662
 Bochanski, J. J., Munn, J. A., Hawley, S. L., et al. 2007, *AJ*, **134**, 2418
 Bonfils, X., Delfosse, X., Udry, S., et al. 2005, *A&A*, **442**, 635
 Bonfils, X., Delfosse, X., Udry, S., et al. 2013, *A&A*, **549**, A109
 Boyajian, T. S., von Braun, K., van Belle, G., et al. 2012, *ApJ*, **757**, 112B
 Browning, M. K. 2008, *ApJ*, **676**, 1262
 Caballero, J. A., Guàrdia, J., López del Fresno, M., et al. 2016, in ObservatoryOperations: Strategies, Processes, and Systems VI, *Proc. SPIE*, **9910**, 99100E
 Casagrande, L., Flynn, C., & Bessell, M. 2008, *MNRAS*, **389**, 585
 Cortés-Contreras, M., Béjar, V. J. S., Caballero, J. A., et al. 2017, *A&A*, **597**, A47
 Cosentino, R., Lovis, C., Pepe, F., et al. 2012, in *SPIE Conf. Ser.*, **8446**, 1
 Delfosse, X., Forveille, T., Beuzit, J.-L., et al. 1999, *A&A*, **344**, 897
 Delfosse, X., Forveille, T., Ségransan, D., et al. 2000, *A&A*, **364**, 217
 Dotter, A., Chaboyer, B., Jevremović, D., et al. 2008, *ApJS*, **178**, 89
 Dressing, C. D., & Charbonneau, D. 2013, *ApJ*, **767**, 95
 Feiden, G. A., Chaboyer, B., & Dotter, A. 2011, *ApJL*, **740**, L25
 Gaia Collaboration et al. 2018, *A&A*, **616**, A1
 Gaia Collaboration et al. 2021, *A&A*, **649**, A1
 Gaidos, E. 2013, *ApJ*, **770**, 90
 Gray, D. F. 1989, *ApJ*, **347**, 1021
 Gray, D. F. 1994, *PASP*, **106**, 1248
 Husser, T.-O., Wende-von Berg, S., Dreizler, S., et al. 2013, *A&A*, **553**, A6
 Hawkins M. R. S., Bessell M. S., 1988, *MNRAS*, **234**, 177
 Hawley, S.L., Gizis, J.E., & Reid, I.N. 1996, *AJ*, **112**, 2799
 Houdebine, É. R., Mullan, D. J., Doyle, J. G., et al. 2019, *AJ*, **158**, 56
 Ida, S., & Lin, D. N. C. 2004, *ApJ*, **604**, 388
 Johnson, J. A., et al. 2012, *AJ*, **143**, 111
 Kaeufl, H. U., Ballester, P., Biereichel, P., et al. 2004, *SPIE*, **5492**, 1218
 Khata, D., Mondal, S., Das, R., et al. 2020, *MNRAS*, **493**, 4533
 Kirkpatrick J. D., McGraw J. T., Hess T. R., et al., 1994, *ApJS*, **94**, 749
 Kovtyukh, V. V., & Gorlova, N. I. 2000, *A&A*, **358**, 587
 Kovtyukh, V. V., Andrievsky, S. M., Luck, R. E., et al. 2003, *A&A*, **401**, 661
 Laughlin, G., Bodenheimer, P., & Adams, F.C. 2004, *ApJ*, **612**, L73
 Leggett, S. K., Allard, F., Berriman, G. et. al. 1996, *ApJS*, **104**, 117
 López-Morales M., Ribas I., 2005, *ApJ*, **631**, 1120
 Maldonado, J., Affer, L., Micela, G., et al., 2015, *A&A*, **577**, A132
 Mallik, S. V. 1994, *A&AS*, **103**, 279
 Mallik, S. V. 1997, *A&AS*, **124**, 359
 Mann, A. W., Brewer, J. M., Gaidos, E., Lépine, S., & Hilton, E. J. 2013a, *AJ*, **145**, 52
 Mann, A. W., Gaidos, E., & Ansdel, M. 2013b, *ApJ*, **779**, 188
 Mann, A. W., Feiden, G. A., Gaidos, E., & Boyajian, T. 2015, *ApJ*, **804**, 64
 Markus, R., Régis, L., Andrés, J., et al. 2019, *MNRAS*, **484**, 2, 2674
 Martinez, A. O., Crossfield, I. J. M., Schlieder, J. E., et al. 2017, *ApJ*, **837**, 72
 Mayor, M., Pepe, F., Queloz, D., et al. 2003, *The Messenger*, **114**, 20
 Mercer, A., & Stamatellos, D. 2020, *A&A*, **633**, A116
 Montes, D., Crespo-Chacón, I., Gálvez, M., & Fernández-Figuerola, M., 2006, *Proceedings of the International Astronomical Union*, **2(S240)**, 690-696

- Morales J. C., Ribas I., Jordi C., 2008, *A&A*, **478**, 507
 Mullan, D. J., & MacDonald, J. 2001, *ApJ*, **559**, 353
 Neves, V., Bonfils, X., Santos, N. C., et al. 2012, *A&A*, **538**, A25
 Neves, V., Bonfils, X., Santos, N. C., et al. 2013, *A&A*, **551**, A36
 Newton, E. R., Charbonneau, D., Irwin, J., Berta-Thompson, Z. K., Rojas-Ayala, B., Covey, K., & Lloyd, J. P. 2014, *AJ*, **147**, 20
 Newton, E. R., Charbonneau, D., Irwin, J., & Mann, A. W. 2015, *ApJ*, **800**, 85
 Newton, E. R., Irwin, J., Charbonneau, D., et al., 2017, *ApJ*, **834**, 85
 Nidever, D. L., Holtzman, J. A., Allende Prieto, C., et al. 2015, *AJ*, **150**, 173
 Nordström, B.; Mayor, M.; Andersen, J., 2004, *A&A*, **418**, 989
 Passegger, V. M., Reiners, A., Jeffers, S. V., et al. 2018, *A&A*, **615**, A6
 Passegger, V. M., Bello-García, A., Ordieres-Meré, J., et al. 2020, *A&A*, **642**, A22
 Pirzkal N. et al., 2005, *ApJ*, **622**, 319
 Rajpurohit, A. S., Allard, F., Rajpurohit, S., et al. 2018, *A&A*, **620**, A180
 Reid, I. N., & Gizis, J. E. 1997, *AJ*, **113**, 2246
 Reid, I. N., Gizis, J. E., & Hawley, S. L., 2002, *AJ*, **124**, 2721
 Reiners, A., Zechmeister, M., Caballero, J. A., et al. 2018, *A&A*, **612**, A49
 Rojas-Ayala, B., Covey, K. R., Muirhead, P. S., & Lloyd, J. P. 2012, *ApJ*, **748**, 93
 Santos, N. C., Bouchy, F., Mayor, M., et al. 2004, *A&A*, **426**, L19
 Sarro, L. M., Ordieres-Meré, J., Bello-García, A., et al. 2018, *MNRAS*, **476**, 1120
 Schlaufman, K. C., & Laughlin, G. 2010, *A&A*, **519**, A105
 Schweitzer, A., Passegger, V. M., Cifuentes, C., et al. 2019, *A&A*, **625**, A68
 Sharma, K., Kembhavi, A., Kembhavi, A., et al. 2019, *MNRAS*, **491**, 2280
 Sousa, S. G., Alapini, A., Israelian, G., et al. 2010, *A&A*, **512**, A13
 Stauffer J. R., Hartmann L. W., 1986, *ApJS*, **61**, 531
 Strassmeier, K. G., & Schordan, P., 2000, *Astronomische Nachrichten*, **321**, 277
 Terrien, R. C., Mahadevan, S., Bender, C. F., Deshpande, R., Ramsey, L. W., & Bochanski, J. J. 2012, *ApJ*, **747**, L38
 Terrien, R. C., Mahadevan, S., Deshpande, R., & Bender, C. F. 2015, *ApJS*, **220**, 16
 Tinney, C. G., & Reid, I. N. 1998, *MNRAS*, **301**, 1031
 Veyette, M. J., Muirhead, P. S., Mann, A. W., et al. 2017, *ApJ*, **851**, 26
 West, A. A., Bochanski, J. J., Hawley, S. L., et al. 2006, *AJ*, **132**, 2507
 Woolf, V., & Wallerstein, G. 2006, *PASP*, **118**, 218
 Zechmeister, M., Anglada-Escudé, G., & Reiners, A. 2014, *A&A*, **561**, A59
 Zheng Z., Flynn C., Gould A., et al., 2001, *ApJ*, **555**, 393
 Zheng Z., Flynn C., Gould A., et al., 2004, *ApJ*, **601**, 500
 Zhou X., 1991, *A&A* **248**, 367

APPENDIX A: CALCULATIONS OF RMSE, MAD AND R_{AP}^2

The root mean squared error (RMSE) is the square root of the variance of the residuals. The RMSE is defined as :

$$RMSE = \sqrt{\sum_{i=1}^n \frac{(\hat{y}_i - y_i)^2}{(n-p)}} \quad (A1)$$

where, n is the number of data points (i.e., number of calibrators), p is the number of predictors used in the model, y_i is the value of the response variable i, and \hat{y}_i is the value predicted by the regression model for given y_i .

The mean absolute deviation (MAD) measures the statistical dispersion or variability in a dataset. The MAD is defined as :

$$MAD = \sum_{i=1}^n \frac{|y_i - \bar{y}|}{n} \quad (A2)$$

where, \bar{y} is the overall mean of the observations y_i .

The adjusted square of the multiple correlation coefficient

(R_{ap}^2) represents the proportion of variability in a data set that is accounted for by a regression model. The R_{ap}^2 is defined as :

$$R_{ap}^2 = 1 - \frac{(n-1) \sum_{i=1}^n (\hat{y}_i - y_i)^2}{(n-p) \sum_{i=1}^n (y_i - \bar{y})^2} \quad (A3)$$

APPENDIX B: TABLES

Table B1. EWs of the selected spectral features and estimated stellar parameters of the CARMENES M-dwarf stars.

Karmn ^(a)	Name	Sp.type ^(b)	Ca I EW (Å) (0.854 μm)	Ca I EW (Å) (0.866 μm)	Mg I EW (Å) (1.57 μm)	$T_{\text{eff}}^{(c)}$ (K)	Radius ^(c) (R_{\odot})	Luminosity ^(c) ($\log L/L_{\odot}$)
J00051+457	GJ 2	M1.0 V	3.491±0.608	2.426±0.375	3.761±0.193	3692±107	0.509±0.067	-1.330±0.224
J00067-075	GJ 1002	M5.5 V	0.577±0.555	1.368±0.355	0.590±0.130	2894±129	0.160±0.069	-2.868±0.232
J00162+198E	GJ 1006B	M4.0 V	1.022±0.505	1.452±0.311	1.060±0.294	3015±108	0.205±0.067	-2.548±0.224
J00183+440	GJ 15A	M1.0 V	3.253±0.430	2.926±0.275	2.123±0.218	3542±104	0.392±0.066	-1.747±0.222
J00184+440	GJ 15B	M3.5 V	2.400±0.523	2.272±0.320	0.730±0.192	3303±110	0.297±0.067	-1.871±0.226
J00286-066	GJ 1012	M4.0 V	1.750±0.598	1.824±0.394	1.856±0.353	3214±128	0.286±0.071	-2.140±0.241
J00389+306	GJ 26	M2.5 V	3.145±0.297	2.314±0.205	2.723±0.142	3552±110	0.422±0.067	-1.613±0.226
J00570+450	G 172-030	M3.0 V	1.908±0.511	2.634±0.321	1.458±0.138	3221±141	0.273±0.072	-2.251±0.250
J01013+613	GJ 47	M2.0 V	2.826±0.479	2.237±0.318	2.326±0.087	3462±119	0.380±0.068	-1.765±0.232
J01025+716	GJ 48	M3.0 V	2.500±0.259	2.417±0.190	2.676±0.245	3420±103	0.368±0.066	-1.835±0.221
J01026+623	GJ 49	M1.5 V	3.699±0.251	3.031±0.176	3.797±0.057	3735±104	0.500±0.066	-1.407±0.221
J01048-181	GJ 1028	M5.0 V	0.459±0.728	0.965±0.461	0.585±0.200	2871±126	0.153±0.067	-2.893±0.223
J01125-169	GJ 54.1	M4.5 V	0.662±0.690	1.780±0.355	0.388±0.117	2900±108	0.162±0.067	-2.830±0.224
J01339-176	LP 768-113	M4.0 V	1.150±0.802	1.534±0.458	1.128±0.226	3044±118	0.216±0.069	-2.487±0.233
J01433+043	GJ 70	M2.0 V	3.167±0.578	2.732±0.302	2.809±0.219	3562±111	0.417±0.068	-1.669±0.227
J01518+644	GJ 3117A	M2.5 V	2.854±0.576	2.402±0.306	3.354±0.386	3540±122	0.434±0.071	-1.582±0.236
J02002+130	GJ 83.1	M3.5 V	1.201±0.599	0.842±0.306	0.532±0.211	3025±108	0.209±0.067	-2.389±0.224
J02015+637	GJ 3126	M3.0 V	2.256±0.522	2.050±0.297	3.204±0.200	3423±120	0.397±0.070	-1.689±0.239
J02070+496	G 173-037	M3.5 V	3.153±0.572	2.440±0.313	1.514±0.179	3496±109	0.371±0.067	-1.732±0.225
J02088+494	GJ 3136	M3.5 V	1.714±0.432	1.365±0.312	2.110±0.218	3228±114	0.315±0.068	-1.960±0.227
J02123+035	GJ 87	M1.5 V	3.211±0.254	2.742±0.202	3.305±0.139	3604±106	0.445±0.067	-1.571±0.223
J02222+478	GJ 96	M0.5 V	3.763±0.197	3.150±0.191	5.078±0.116	3855±107	0.584±0.068	-1.154±0.225
J02336+249	GJ 102	M4.0 V	1.283±0.577	1.008±0.362	1.121±0.247	3071±124	0.236±0.068	-2.314±0.228
J02358+202	GJ 104	M2.0 V	3.621±0.455	3.036±0.314	3.113±0.099	3674±112	0.458±0.069	-1.543±0.229
J02362+068	GJ 105B	M4.0 V	2.124±0.488	1.859±0.330	1.098±0.067	3251±114	0.286±0.068	-2.082±0.228
J02442+255	GJ 109	M3.0 V	2.495±0.221	2.445±0.224	1.579±0.093	3353±110	0.323±0.067	-1.992±0.226
J02519+224	RBS 365	M4.0 V	1.598±0.348	1.129±0.381	1.475±0.135	3157±129	0.276±0.070	-2.117±0.236
J02530+168	Teegarden's Star	M7.0 V	1.174±0.426	1.198±0.371	0.216±0.102	3012±130	0.200±0.071	-2.163±0.242
J02565+554W	GJ 119A	M1.0 V	4.133±0.461	3.128±0.388	4.819±0.303	3897±103	0.595±0.067	-1.123±0.221
J03181+382	GJ 134	M1.5 V	4.004±0.214	3.057±0.182	5.309±0.293	3917±115	0.626±0.069	-1.027±0.231
J03213+799	GJ 133	M2.0 V	2.988±0.368	2.455±0.317	3.075±0.149	3544±106	0.425±0.067	-1.619±0.223
J03217-066	GJ 3218	M2.0 V	3.274±0.354	2.536±0.312	2.626±0.139	3573±108	0.421±0.068	-1.632±0.224
J03463+262	GJ 154	M0.0 V	4.141±0.439	3.458±0.398	4.320±0.186	3859±119	0.548±0.069	-1.285±0.232
J03473-019	G 080-021	M3.0 V	1.902±0.378	1.648±0.308	2.736±0.286	3319±120	0.359±0.068	-1.800±0.229
J03531+625	Ross 567	M3.0 V	1.115±0.231	0.618±0.151	2.573±0.070	3208±119	0.442±0.066	-1.410±0.221
J04225+105	LSPM J0422+1031	M3.5 V	2.184±0.467	1.958±0.297	2.195±0.262	3323±119	0.332±0.067	-1.943±0.227
J04290+219	GJ 169	M0.5 V	4.538±0.130	3.200±0.090	6.685±0.101	4141±105	0.776±0.066	-0.642±0.221
J04376+528	GJ 172	M0.0 V	4.393±0.310	3.530±0.202	4.971±0.246	3957±108	0.604±0.067	-1.122±0.225
J04376-110	GJ 173	M1.5 V	3.528±0.171	2.986±0.103	2.801±0.125	3636±107	0.438±0.067	-1.605±0.223
J04429+189	GJ 176	M2.0 V	3.325±0.240	2.757±0.141	2.740±0.261	3590±106	0.425±0.067	-1.637±0.223
J04429+214	2M J04425586+21282305	M3.5 V	1.816±0.441	2.403±0.303	1.746±0.120	3219±117	0.277±0.068	-2.229±0.228
J04472+206	RX J0447.2+2038	M5.0 V	0.610±0.842	0.879±0.472	0.697±0.112	2908±107	0.169±0.066	-2.749±0.222
J04520+064	GJ 179	M3.5 V	2.427±0.470	1.615±0.299	2.353±0.301	3382±111	0.373±0.068	-1.738±0.227
J04538-177	GJ 180	M2.0 V	3.077±0.276	2.435±0.173	3.413±0.186	3587±113	0.454±0.068	-1.518±0.225
J04588+498	GJ 181	M0.0 V	4.242±0.157	3.433±0.103	5.808±0.114	4005±112	0.658±0.068	-0.963±0.225
J05019+011	1RXS J050156.7+010845	M4.0 V	1.340±0.430	1.228±0.252	1.665±0.178	3123±124	0.264±0.067	-2.192±0.223
J05019-069	GJ 3323	M4.0 V	1.284±0.476	2.081±0.314	0.598±0.108	3046±112	0.211±0.068	-2.471±0.227
J05033-173	GJ 3325	M3.0 V	2.677±0.440	1.906±0.281	1.582±0.287	3393±124	0.343±0.072	-1.849±0.253
J05062+046	RX J0506.2+0439	M4.0 V	1.447±0.499	1.217±0.289	1.015±0.170	3099±110	0.239±0.067	-2.309±0.226
J05127+196	GJ 192	M2.0 V	3.151±0.416	2.420±0.269	2.771±0.196	3556±109	0.422±0.068	-1.624±0.228
J05280+096	GJ 203	M3.5 V	1.980±0.445	2.024±0.291	1.271±0.397	3227±112	0.279±0.068	-2.167±0.228
J05314-036	GJ 205	M1.5 V	3.656±0.174	3.209±0.121	4.829±0.194	3813±105	0.555±0.067	-1.246±0.223
J05337+019	GJ 207.1	M2.5 V	1.948±0.429	1.775±0.259	2.547±0.418	3308±122	0.342±0.069	-1.883±0.232
J05348+138	GJ 3356	M3.5 V	1.730±0.425	2.127±0.265	1.979±0.198	3220±114	0.284±0.068	-2.176±0.229
J05360-076	GJ 3357	M4.0 V	2.124±0.503	1.746±0.280	1.465±0.247	3267±116	0.299±0.069	-2.052±0.231
J05365+113	GJ 208	M0.0 V	4.006±0.145	3.320±0.107	5.283±0.127	3915±106	0.608±0.068	-1.098±0.225
J05366+112	2M J05363846+1117487	M4.0 V	1.347±0.521	1.208±0.277	1.400±0.209	3103±117	0.250±0.068	-2.265±0.230
J05421+124	GJ 213	M4.0 V	1.240±0.482	1.779±0.271	1.176±0.247	3066±110	0.222±0.067	-2.473±0.225
J06000+027	GJ 3379	M4.0 V	1.100±0.413	1.732±0.241	1.008±0.146	3026±106	0.207±0.067	-2.559±0.223
J06011+595	GJ 3378	M3.5 V	2.171±0.467	1.840±0.247	2.185±0.448	3320±109	0.334±0.068	-1.923±0.225
J06103+821	GJ 226	M2.0 V	2.873±0.239	2.620±0.162	2.324±0.137	3472±103	0.375±0.066	-1.813±0.221
J06105-218	GJ 229A	M0.5 V	3.776±0.216	3.063±0.120	4.399±0.137	3796±103	0.542±0.066	-1.276±0.221
J06246+234	GJ 232	M4.0 V	1.642±1.132	0.796±0.540	0.433±0.623	3123±122	0.240±0.069	-2.024±0.236
J06371+175	GJ 239	M0.0 V	3.547±0.285	2.707±0.170	2.924±0.113	3647±106	0.452±0.067	-1.537±0.222
J06396-210	LP 780-032	M4.0 V	2.510±0.471	1.523±0.208	2.072±0.191	3381±118	0.365±0.068	-1.752±0.230

(continued on next page ..)

Table B1 – continued from the previous page.

Karmn ^(a)	Name	Sp.type ^(b)	Ca I EW (Å) (0.854 μm)	Ca I EW (Å) (0.866 μm)	Mg I EW (Å) (1.57 μm)	$T_{eff}^{(c)}$ (K)	Radius ^(c) (R_{\odot})	Luminosity ^(c) ($\log L/L_{\odot}$)
J06421+035	GJ 3404A	M3.5 V	3.090±0.602	2.486±0.346	1.820±0.099	3493±117	0.375±0.068	-1.766±0.230
J06548+332	GJ 251	M3.0 V	2.532±0.567	2.160±0.316	1.683±0.282	3366±114	0.332±0.068	-1.936±0.229
J06574+740	2M J06572616+7405265	M4.0 V	2.104±0.529	1.521±0.310	1.896±0.126	3287±124	0.324±0.068	-1.933±0.228
J07033+346	GJ 3423	M4.0 V	2.160±0.498	1.426±0.296	1.526±0.135	3278±121	0.311±0.069	-1.964±0.234
J07044+682	GJ 258	M3.0 V	2.192±0.636	2.015±0.381	2.459±0.224	3345±122	0.345±0.070	-1.893±0.236
J07274+052	GJ 273	M3.5 V	2.201±0.263	1.871±0.156	0.666±0.044	3256±113	0.282±0.068	-1.924±0.228
J07287-032	GJ 1097	M3.0 V	2.837±0.499	1.913±0.320	2.772±0.103	3493±111	0.418±0.067	-1.597±0.223
J07319+362N	GJ 277C	M3.5 V	1.898±0.466	1.978±0.328	1.623±0.133	3228±109	0.285±0.067	-2.158±0.225
J07353+548	GJ 3452	M2.0 V	2.929±0.328	2.474±0.310	2.423±0.391	3489±117	0.387±0.069	-1.758±0.232
J07361-031	GJ 282C	M1.0 V	3.247±0.178	2.561±0.178	3.950±0.177	3662±107	0.497±0.067	-1.382±0.224
J07386-212	GJ 3459	M3.0 V	2.596±0.325	2.205±0.324	2.089±0.398	3400±115	0.352±0.068	-1.872±0.230
J07393+021	GJ 281	M0.0 V	4.329±0.235	3.435±0.211	4.928±0.069	3942±108	0.601±0.067	-1.125±0.225
J07472+503	2M J07471385+5020386	M4.0 V	2.193±0.269	1.664±0.316	1.500±0.158	3284±109	0.307±0.067	-2.006±0.224
J07558+833	GJ 1101	M4.5 V	1.313±0.297	1.025±0.367	1.437±0.216	3099±109	0.256±0.067	-2.208±0.224
J07582+413	GJ 1105	M3.5 V	2.550±0.305	1.257±0.358	2.172±0.172	3396±108	0.390±0.067	-1.620±0.224
J08119+087	GJ 299	M4.5 V	2.098±0.318	1.759±0.415	1.107±0.150	3246±109	0.285±0.067	-2.082±0.223
J08126-215	GJ 300	M4.0 V	1.118±0.265	1.443±0.368	1.849±0.419	3106±103	0.250±0.066	-2.278±0.220
J08161+013	GJ 2066	M2.0 V	3.431±0.183	2.750±0.196	2.449±0.187	3597±103	0.420±0.066	-1.641±0.221
J08293+039	2M J08292191+0355092	M2.5 V	2.991±0.166	2.144±0.220	3.318±0.144	3563±102	0.455±0.066	-1.487±0.220
J08315+730	LP 035-219	M4.0 V	1.772±0.328	1.496±0.431	1.693±0.115	3207±104	0.289±0.066	-2.097±0.222
J08358+680	GJ 3506	M2.5 V	2.756±0.246	1.946±0.344	1.964±0.180	3428±116	0.365±0.067	-1.788±0.221
J08402+314	LSPM J0840+3127	M3.5 V	2.538±0.246	2.091±0.381	1.317±0.199	3352±104	0.322±0.066	-1.935±0.222
J08413+594	GJ 3512	M5.5 V	0.566±0.423	1.164±0.639	0.107±0.204	2870±108	0.153±0.067	-2.606±0.225
J09005+465	GJ 1119	M4.5 V	2.158±0.282	1.456±0.404	1.292±0.263	3267±118	0.300±0.068	-2.002±0.231
J09028+680	GJ 3526	M4.0 V	2.139±0.252	1.835±0.412	1.549±0.163	3274±116	0.302±0.068	-2.051±0.231
J09133+688	G 234-057	M2.5 V	3.265±0.240	2.778±0.413	2.500±0.200	3564±111	0.409±0.067	-1.690±0.226
J09140+196	LP 427-016	M3.0 V	2.528±0.248	2.394±0.420	2.228±0.188	3395±114	0.349±0.068	-1.905±0.229
J09161+018	RX J0916.1+0153	M4.0 V	1.054±0.364	1.257±0.683	1.623±0.181	3072±117	0.238±0.069	-2.325±0.236
J09163-186	GJ 3543	M1.5 V	3.338±0.208	2.527±0.383	3.300±0.309	3629±105	0.462±0.067	-1.493±0.222
J09307+003	GJ 1125	M3.5 V	2.387±0.231	2.455±0.451	1.557±0.267	3328±117	0.314±0.068	-2.036±0.227
J09360-216	GJ 357	M2.5 V	2.474±0.204	2.294±0.382	2.394±0.435	3395±105	0.355±0.066	-1.875±0.221
J09411+132	GJ 361	M1.5 V	3.115±0.193	2.624±0.244	2.743±0.115	3547±103	0.412±0.066	-1.677±0.221
J09423+559	GJ 363	M3.5 V	2.190±0.211	1.883±0.397	1.510±0.093	3283±113	0.304±0.067	-2.043±0.224
J09425+700	GJ 360	M2.0 V	3.192±0.124	2.680±0.257	2.773±0.354	3564±102	0.418±0.066	-1.659±0.220
J09428+700	GJ 362	M3.0 V	2.985±0.142	2.206±0.244	2.171±0.113	3487±112	0.386±0.068	-1.730±0.228
J09439+269	GJ 3564	M3.5 V	2.680±0.302	2.355±0.343	1.439±0.117	3388±107	0.333±0.067	-1.909±0.224
J09447-182	GJ 1129	M4.0 V	1.465±0.469	1.767±0.521	1.180±0.184	3112±128	0.239±0.070	-2.370±0.243
J09468+760	GJ 366	M1.5 V	3.405±0.168	2.760±0.196	3.914±0.185	3688±106	0.496±0.067	-1.400±0.225
J09511-123	GJ 369	M0.5 V	3.728±0.155	2.907±0.193	3.390±0.279	3713±107	0.484±0.067	-1.448±0.226
J09561+627	GJ 373	M0.0 V	4.003±0.160	3.502±0.191	4.874±0.132	3878±106	0.570±0.067	-1.221±0.224
J10023+480	GJ 378	M1.0 V	3.949±0.251	2.947±0.296	4.633±0.182	3847±113	0.577±0.068	-1.160±0.233
J10122-037	GJ 382	M1.5 V	3.331±0.104	2.060±0.122	3.883±0.088	3672±104	0.531±0.066	-1.227±0.221
J10125+570	LP 092-048	M3.5 V	2.718±0.268	1.663±0.315	1.784±0.304	3411±114	0.360±0.068	-1.768±0.231
J10167-119	GJ 386	M3.0 V	2.709±0.252	2.540±0.305	3.597±0.242	3536±116	0.433±0.068	-1.596±0.233
J10251-102	GJ 390	M1.0 V	3.444±0.146	2.956±0.187	3.872±0.158	3692±108	0.488±0.067	-1.441±0.225
J10289+008	GJ 393	M2.0 V	3.210±0.149	2.745±0.136	2.784±0.077	3569±107	0.418±0.067	-1.663±0.224
J10350-094	LP 670-017	M3.0 V	2.596±0.288	2.112±0.330	2.547±0.491	3429±108	0.378±0.067	-1.770±0.226
J10396-069	GJ 399	M2.5 V	2.539±0.170	2.732±0.212	2.699±0.203	3429±104	0.364±0.066	-1.874±0.222
J10504+331	GJ 3626	M4.0 V	1.976±0.379	1.874±0.533	2.262±0.265	3289±126	0.323±0.069	-1.976±0.235
J10508+068	GJ 402	M4.0 V	1.425±0.259	1.466±0.395	0.577±0.190	3077±113	0.223±0.068	-2.332±0.228
J11000+228	GJ 408	M2.5 V	2.774±0.174	2.752±0.299	1.869±0.095	3427±102	0.350±0.066	-1.908±0.220
J11026+219	GJ 410	M2.0 V	3.354±0.119	2.544±0.237	4.553±0.139	3736±104	0.552±0.066	-1.206±0.221
J11033+359	GJ 411	M1.5 V	2.616±0.062	2.040±0.144	2.775±0.027	3450±103	0.395±0.066	-1.695±0.220
J11054+435	GJ 412A	M1.0 V	3.565±0.147	2.856±0.381	2.219±0.106	3615±107	0.420±0.067	-1.630±0.224
J11110+304	GJ 414B	M2.0 V	4.835±0.118	3.853±0.323	6.871±0.127	4207±104	0.759±0.066	-0.726±0.222
J11126+189	GJ 3649	M1.5 V	3.647±0.279	2.728±0.736	3.311±0.295	3691±112	0.479±0.067	-1.450±0.226
J11201-104	LP 733-099	M2.0 V	2.806±0.258	2.361±0.715	3.156±0.162	3515±107	0.420±0.067	-1.631±0.225
J11289+101	GJ 3666	M3.5 V	2.348±0.263	1.926±0.744	1.396±0.175	3313±113	0.311±0.068	-1.994±0.229
J11302+076	K2-18	M2.5 V	3.053±0.387	2.454±1.059	1.958±0.286	3491±105	0.377±0.066	-1.767±0.222
J11306-080	LP 672-042	M3.5 V	2.557±0.239	1.843±0.676	1.794±0.112	3376±122	0.344±0.069	-1.863±0.237
J11417+427	GJ 1148	M4.0 V	1.468±0.263	1.954±0.797	1.176±0.244	3112±107	0.238±0.067	-2.392±0.224
J11421+267	GJ 436	M2.5 V	2.593±0.197	2.072±0.578	2.104±0.079	3401±118	0.356±0.068	-1.847±0.234
J11467-140	GJ 443	M3.0 V	3.012±0.237	1.784±0.715	3.592±0.288	3589±107	0.505±0.067	-1.286±0.228
J11476+002	GJ 3685A	M4.0 V	0.968±0.284	1.867±0.917	1.197±0.433	3015±116	0.201±0.068	-2.603±0.231

(continued on next page ..)
MNRAS **000**, 1–12 (2021)

Table B1 – continued from the previous page.

Karmn ^(a)	Name	Sp.type ^(b)	Ca I EW (Å) (0.854 μm)	Ca I EW (Å) (0.866 μm)	Mg I EW (Å) (1.57 μm)	$T_{\text{eff}}^{(c)}$ (K)	Radius ^(c) (R_{\odot})	Luminosity ^(c) (log L/L_{\odot})
J11476+786	GJ 445	M3.5 V	2.199±0.254	1.614±0.742	1.755±0.136	3298±111	0.321±0.067	-1.952±0.226
J11477+008	GJ 447	M4.0 V	3.043±0.252	2.786±0.734	2.907±0.346	3543±109	0.411±0.067	-1.698±0.225
J11509+483	GJ 1151	M4.5 V	1.344±0.265	1.295±0.783	0.654±0.255	3062±107	0.220±0.067	-2.384±0.224
J11511+352	GJ 450	M1.5 V	3.492±0.197	2.895±0.577	2.756±0.204	3626±105	0.435±0.067	-1.607±0.222
J12054+695	GJ 3704	M4.0 V	1.132±0.365	1.997±1.027	0.909±0.338	3027±108	0.205±0.067	-2.580±0.224
J12100-150	GJ 3707	M3.5 V	2.420±0.300	1.933±0.806	1.903±0.217	3353±109	0.337±0.067	-1.913±0.224
J12111-199	GJ 3708A	M3.0 V	2.964±0.195	2.479±0.520	2.589±0.207	3506±105	0.397±0.067	-1.722±0.222
J12123+544S	GJ 458A	M0.0 V	3.970±0.159	2.856±0.429	5.066±0.135	3889±113	0.618±0.069	-1.035±0.227
J12156+526	StKM 2-809	M4.0 V	2.146±0.268	1.633±0.696	1.830±0.194	3292±111	0.320±0.067	-1.961±0.224
J12189+111	GJ 1156	M5.0 V	0.849±0.393	1.217±0.992	0.025±0.228	2935±108	0.174±0.067	-0.865±0.224
J12230+640	GJ 463	M3.0 V	2.959±0.415	2.590±1.084	2.746±0.202	3515±114	0.401±0.069	-1.717±0.228
J12248-182	GJ 465	M2.0 V	3.457±0.290	2.746±0.752	1.718±0.321	3571±104	0.397±0.067	-1.659±0.222
J12312+086	GJ 471	M0.5 V	4.129±0.291	2.588±0.731	4.746±0.146	3890±123	0.624±0.071	-0.996±0.231
J12350+098	GJ 476	M2.5 V	3.434±0.261	2.579±0.624	3.084±0.226	3633±106	0.455±0.067	-1.519±0.222
J12373-208	LP 795-038	M4.0 V	2.050±0.458	1.658±1.152	1.639±0.285	3261±112	0.303±0.068	-2.039±0.227
J12388+116	GJ 480	M3.0 V	2.296±0.297	2.056±0.742	2.567±0.136	3373±105	0.358±0.067	-1.844±0.222
J12428+418	G 123-055	M4.0 V	1.304±0.351	1.941±0.937	0.396±0.337	3045±106	0.211±0.067	-2.339±0.223
J12479+097	GJ 486	M3.5 V	2.388±0.348	1.633±0.791	1.564±0.312	3329±105	0.326±0.067	-1.915±0.223
J13005+056	GJ 493.1	M4.5 V	1.088±0.384	0.709±0.774	0.965±0.448	3021±117	0.223±0.068	-2.349±0.227
J13102+477	G 177-025	M5.0 V	1.261±0.652	1.233±1.300	0.717±0.214	3045±114	0.215±0.068	-2.430±0.228
J13196+333	GJ 507.1	M1.5 V	3.532±0.303	3.223±0.635	3.857±0.221	3707±105	0.484±0.067	-1.473±0.223
J13209+342	GJ 508.2	M1.0 V	3.507±0.223	2.900±0.393	4.153±0.134	3727±104	0.513±0.066	-1.355±0.221
J13229+244	GJ 3779	M4.0 V	2.081±0.373	2.146±0.652	0.822±0.079	3233±106	0.275±0.067	-2.081±0.222
J13283-023W	GJ 512A	M3.0 V	2.697±0.226	1.797±0.378	2.983±0.159	3481±111	0.429±0.066	-1.548±0.221
J13293+114	GJ 513	M3.5 V	2.948±0.427	2.424±0.637	2.249±0.443	3483±107	0.382±0.067	-1.769±0.223
J13299+102	GJ 514	M0.5 V	3.537±0.167	3.146±0.274	3.341±0.111	3671±103	0.460±0.066	-1.548±0.220
J13427+332	GJ 3801	M3.5 V	1.948±0.524	1.573±0.638	1.186±0.202	3216±107	0.278±0.067	-2.123±0.224
J13450+176	GJ 525	M1.0 V	3.694±0.295	3.163±0.342	3.359±0.138	3704±103	0.472±0.066	-1.506±0.221
J13457+148	GJ 526	M1.5 V	3.438±0.266	2.114±0.280	3.524±0.090	3664±105	0.506±0.067	-1.309±0.222
J13458-179	GJ 3804	M3.5 V	2.890±0.658	2.275±0.667	1.558±0.113	3439±111	0.354±0.068	-1.818±0.228
J13536+776	RX J1353.6+7737	M4.0 V	1.514±0.661	1.320±0.665	0.630±0.358	3099±113	0.232±0.068	-2.278±0.229
J13582+125	GJ 3817	M3.0 V	1.880±0.599	2.310±0.619	0.707±0.161	3184±114	0.258±0.068	-2.162±0.230
J14010-026	GJ 536	M1.0 V	3.357±0.349	2.766±0.343	3.848±0.143	3674±105	0.488±0.066	-1.427±0.221
J14082+805	GJ 540	M1.0 V	3.673±0.504	3.074±0.464	4.530±0.437	3789±114	0.542±0.070	-1.275±0.235
J14152+450	GJ 3836	M3.0 V	2.183±0.662	2.521±0.595	2.041±0.248	3313±118	0.314±0.070	-2.068±0.234
J14173+454	RX J1417.3+4525	M5.0 V	1.215±1.670	1.532±1.172	0.031±0.351	3020±111	0.202±0.067	-0.114±0.227
J14251+518	GJ 549B	M2.5 V	3.159±0.475	2.024±0.380	2.314±0.164	3532±108	0.410±0.067	-1.617±0.224
J14257+236E	GJ 548B	M0.5 V	4.243±0.416	3.348±0.327	4.938±0.175	3927±106	0.600±0.067	-1.124±0.222
J14257+236W	GJ 548A	M0.0 V	4.295±0.368	3.526±0.297	5.366±0.150	3973±104	0.624±0.066	-1.066±0.221
J14294+155	GJ 552	M2.0 V	3.492±0.659	2.738±0.526	3.046±0.306	3643±108	0.453±0.067	-1.539±0.226
J14307-086	GJ 553	M0.5 V	4.218±0.491	3.229±0.361	6.351±0.135	4056±103	0.718±0.066	-0.791±0.221
J14310-122	GJ 553.1	M3.5 V	2.066±0.771	1.911±0.531	1.630±0.181	3263±104	0.299±0.066	-2.081±0.221
J14342-125	GJ 555	M4.0 V	1.854±0.785	1.508±0.486	2.160±0.201	3258±108	0.322±0.066	-1.945±0.220
J14524+123	GJ 3871	M2.0 V	2.975±0.707	2.322±0.467	3.215±0.281	3552±104	0.438±0.066	-1.562±0.220
J14544+355	GJ 3873	M3.5 V	2.385±0.858	2.336±0.576	1.449±0.192	3323±117	0.312±0.068	-2.027±0.231
J15013+055	GJ 3885	M3.0 V	2.014±0.559	2.462±0.401	1.710±0.290	3257±110	0.290±0.067	-2.167±0.226
J15095+031	GJ 3892	M3.0 V	3.016±0.703	2.323±0.467	2.929±0.132	3539±114	0.424±0.067	-1.613±0.226
J15194-077	GJ 581	M3.0 V	2.424±0.461	2.162±0.308	1.722±0.293	3344±108	0.325±0.067	-1.974±0.224
J15218+209	GJ 9520	M1.5 V	2.157±0.420	1.992±0.286	3.664±0.373	3460±122	0.429±0.072	-1.562±0.231
J15369-141	GJ 592	M4.0 V	2.345±0.985	2.076±0.635	2.072±0.069	3347±109	0.336±0.067	-1.937±0.225
J15499+796	LP 022-420	M5.0 V	1.152±1.329	0.509±0.823	0.956±0.258	3034±113	0.239±0.068	-2.211±0.227
J15598-082	GJ 606	M1.0 V	3.287±0.432	2.669±0.292	3.950±0.348	3669±104	0.494±0.067	-1.399±0.222
J16028+205	GJ 609	M4.0 V	2.514±0.691	1.411±0.434	1.177±0.303	3341±106	0.323±0.067	-1.840±0.224
J16092+093	G 137-084	M3.0 V	2.474±0.648	2.099±0.428	2.186±0.152	3381±105	0.350±0.066	-1.877±0.222
J16167+672N	GJ 617B	M3.0 V	2.908±0.375	2.355±0.242	2.928±0.113	3518±104	0.414±0.066	-1.651±0.221
J16167+672S	GJ 617A	M0.0 V	4.421±0.590	3.784±0.412	6.344±0.346	4087±106	0.691±0.068	-0.898±0.225
J16254+543	GJ 625	M1.5 V	3.010±0.309	2.018±0.205	1.875±0.184	3478±103	0.378±0.066	-1.722±0.221
J16303-126	GJ 628	M3.5 V	2.548±0.303	1.753±0.182	1.528±0.212	3362±104	0.334±0.066	-1.878±0.222
J16327+126	GJ 1203	M3.0 V	3.019±0.574	2.529±0.404	2.463±0.109	3510±112	0.394±0.068	-1.734±0.227
J16462+164	GJ 3972	M2.5 V	2.439±0.352	2.417±0.236	2.232±0.432	3377±107	0.342±0.067	-1.937±0.224
J16554-083N	GJ 643	M3.5 V	2.035±0.792	1.373±0.515	1.356±0.145	3243±106	0.295±0.067	-2.030±0.223
J16570-043	GJ 1207	M3.5 V	1.724±0.516	1.311±0.402	1.587±0.174	3190±125	0.285±0.070	-2.093±0.237
J16581+257	GJ 649	M1.0 V	3.399±0.263	2.753±0.211	3.523±0.035	3657±107	0.472±0.067	-1.481±0.224
J17033+514	GJ 3988	M4.5 V	0.919±0.561	1.364±0.411	0.563±0.161	2964±119	0.185±0.069	-2.648±0.233
J17052-050	GJ 654	M1.5 V	3.631±0.338	2.992±0.268	2.895±0.105	3663±110	0.450±0.067	-1.563±0.226

(continued on next page ..)

Table B1 – continued from the previous page.

Karmn ^(a)	Name	Sp.type ^(b)	Ca I EW (Å) (0.854 μm)	Ca I EW (Å) (0.866 μm)	Mg I EW (Å) (1.57 μm)	$T_{eff}^{(c)}$ (K)	Radius ^(c) (R_\odot)	Luminosity ^(c) (log L/L_\odot)
J17071+215	GJ 655	M3.0 V	2.326±0.563	2.224±0.428	2.536±0.180	3376±120	0.353±0.069	-1.879±0.234
J17115+384	GJ 3992	M3.5 V	2.622±0.361	1.751±0.248	2.164±0.093	3410±114	0.370±0.068	-1.756±0.225
J17166+080	GJ 2128	M2.0 V	3.186±0.557	1.897±0.396	2.543±0.233	3550±112	0.430±0.068	-1.538±0.228
J17198+417	GJ 671	M2.5 V	2.872±0.574	2.012±0.422	2.188±0.803	3464±119	0.383±0.070	-1.728±0.233
J17303+055	GJ 678.1 A	M0.0 V	3.419±0.308	2.306±0.214	4.081±0.105	3704±112	0.383±0.068	-1.236±0.227
J17355+616	GJ 685	M0.5 V	3.573±0.298	2.964±0.203	4.923±0.118	3808±107	0.570±0.068	-1.184±0.225
J17378+185	GJ 686	M1.0 V	3.570±0.301	2.776±0.175	3.228±0.107	3670±105	0.467±0.067	-1.494±0.223
J17542+073	GJ 1222	M4.0 V	1.955±0.732	1.765±0.467	1.398±0.300	3227±121	0.284±0.069	-2.132±0.235
J17578+046	GJ 699	M3.5 V	0.160±0.290	0.642±0.159	1.473±0.085	3256±111	0.200±0.066	-2.455±0.220
J17578+465	GJ 4040	M2.5 V	2.747±0.689	2.085±0.396	2.329±0.089	3446±117	0.378±0.069	-1.760±0.235
J18022+642	LP 071-082	M5.0 V	1.283±0.960	0.840±0.547	0.485±0.170	3043±112	0.214±0.068	-2.320±0.228
J18051-030	GJ 701	M1.0 V	3.581±0.221	3.037±0.147	2.777±0.143	3646±106	0.440±0.067	-1.599±0.223
J18174+483	TYC 3529-1437-1	M2.0 V	2.834±0.282	2.133±0.182	3.654±0.127	3563±112	0.469±0.068	-1.438±0.226
J18180+387E	GJ 4048A	M3.0 V	2.531±0.449	2.490±0.337	1.026±0.167	3340±112	0.312±0.068	-1.934±0.228
J18189+661	GJ 4053	M4.5 V	1.463±0.491	1.501±0.339	0.283±0.246	3080±115	0.222±0.068	-2.036±0.230
J18221+063	GJ 712	M4.0 V	2.849±0.484	2.448±0.337	1.676±0.160	3434±114	0.352±0.068	-1.854±0.230
J18224+620	GJ 1227	M4.0 V	1.528±0.455	1.056±0.335	0.767±0.180	3107±112	0.239±0.068	-2.252±0.228
J18319+406	GJ 4062	M3.5 V	2.766±0.428	2.431±0.372	1.582±0.351	3412±115	0.343±0.069	-1.885±0.231
J18346+401	GJ 4063	M3.5 V	1.823±0.368	1.303±0.285	2.347±0.075	3269±118	0.346±0.068	-1.821±0.227
J18353+457	GJ 720A	M0.5 V	4.069±0.197	3.264±0.163	5.334±0.108	3931±121	0.620±0.072	-1.060±0.236
J18363+136	GJ 4065	M4.0 V	2.093±0.333	2.228±0.269	1.539±0.467	3264±120	0.293±0.069	-2.127±0.231
J18409-133	GJ 724	M1.0 V	3.522±0.206	2.960±0.173	4.598±0.077	3768±103	0.542±0.066	-1.268±0.221
J18419+318	GJ 4070	M3.0 V	2.350±0.370	2.210±0.311	2.026±0.133	3346±103	0.331±0.066	-1.967±0.221
J18480-145	GJ 4077	M2.5 V	2.445±0.388	2.109±0.320	2.254±0.276	3379±107	0.351±0.067	-1.876±0.223
J18498-238	GJ 729	M3.5 V	1.898±0.228	2.323±0.200	1.225±0.281	3207±107	0.269±0.067	-2.235±0.224
J18580+059	GJ 740	M0.5 V	3.757±0.213	2.903±0.172	4.842±0.331	3831±112	0.581±0.068	-1.146±0.228
J19070+208	GJ 745A	M2.0 V	3.224±0.280	2.773±0.238	1.594±0.264	3514±116	0.375±0.069	-1.742±0.232
J19072+208	GJ 745B	M2.0 V	3.083±0.412	2.758±0.387	1.660±0.385	3485±125	0.367±0.070	-1.798±0.239
J19084+322	GJ 4098	M3.0 V	2.035±0.403	2.409±0.353	1.690±0.216	3260±120	0.292±0.070	-2.156±0.235
J19098+176	GJ 1232	M4.5 V	1.330±0.494	1.882±0.416	0.331±0.344	3050±105	0.212±0.067	-2.245±0.223
J19169+051N	GJ 752A	M2.5 V	3.094±0.203	2.806±0.174	2.667±0.343	3538±107	0.403±0.067	-1.724±0.224
J19216+208	GJ 1235	M4.5 V	1.082±0.501	1.110±0.367	0.687±0.162	3005±113	0.202±0.068	-2.517±0.226
J19251+283	GJ 4109	M3.0 V	2.087±0.434	1.873±0.361	1.811±0.255	3278±125	0.309±0.071	-2.037±0.238
J19346+045	GJ 763	M0.0 V	4.063±0.217	3.351±0.189	5.803±0.147	3975±108	0.650±0.068	-0.980±0.225
J19511+464	GJ 1243	M4.0 V	1.624±0.412	1.532±0.367	1.079±0.273	3141±113	0.251±0.068	-2.273±0.228
J20260+585	GJ 1253	M5.0 V	1.511±0.781	1.421±0.698	1.091±0.263	3117±106	0.244±0.067	-2.307±0.226
J20305+654	GJ 793	M2.5 V	2.417±0.263	2.413±0.236	1.874±0.112	3351±109	0.327±0.067	-1.994±0.224
J20336+617	GJ 1254	M4.0 V	1.373±0.434	1.403±0.398	2.357±0.271	3200±106	0.306±0.067	-2.001±0.222
J20405+154	GJ 1256	M4.5 V	0.962±0.444	0.602±0.381	0.905±0.103	2992±111	0.214±0.067	-2.385±0.226
J20450+444	GJ 806	M1.5 V	3.245±0.256	2.437±0.259	2.856±0.061	3580±112	0.433±0.067	-1.585±0.224
J20525-169	LP 816-060	M4.0 V	1.139±0.423	1.361±0.457	1.479±0.183	3071±122	0.234±0.068	-2.368±0.229
J20533+621	GJ 809A	M0.5 V	3.887±0.187	3.028±0.188	4.644±0.126	3837±111	0.569±0.067	-1.192±0.223
J20567-104	GJ 811.1	M2.5 V	2.892±0.650	2.601±0.673	2.700±0.219	3499±110	0.394±0.067	-1.746±0.226
J21019-063	GJ 816	M2.5 V	2.334±0.401	2.478±0.435	2.603±0.175	3383±105	0.350±0.066	-1.911±0.222
J21152+257	GJ 4184	M3.0 V	2.957±0.451	2.571±0.469	3.586±0.237	3579±115	0.450±0.068	-1.542±0.226
J21164+025	LSPM J2116+0234	M3.0 V	2.989±0.425	2.296±0.428	2.365±0.326	3498±111	0.393±0.067	-1.717±0.223
J21348+515	GJ 4205	M3.0 V	2.506±0.400	2.246±0.421	2.660±0.309	3420±112	0.373±0.067	-1.802±0.225
J21463+382	LSPM J2146+3813	M4.0 V	2.390±0.467	1.922±0.453	1.151±0.137	3313±111	0.307±0.067	-1.970±0.225
J21466+668	G 264-012	M4.0 V	2.065±0.413	2.138±0.444	1.636±0.043	3264±109	0.295±0.067	-2.115±0.225
J22012+283	GJ 4247	M4.0 V	1.357±0.419	1.441±0.429	1.270±0.169	3095±113	0.239±0.068	-2.349±0.228
J22020-194	GJ 843	M3.5 V	2.013±0.387	1.668±0.478	2.613±0.185	3326±119	0.357±0.068	-1.811±0.228
J22021+014	GJ 846	M0.5 V	3.772±0.193	2.864±0.236	4.570±0.145	3810±104	0.564±0.067	-1.194±0.222
J22057+656	GJ 4258	M1.5 V	3.047±0.286	2.710±0.388	3.310±0.155	3573±109	0.434±0.067	-1.608±0.225
J22096-046	GJ 849	M3.5 V	2.742±0.180	1.906±0.296	3.303±0.115	3516±105	0.450±0.066	-1.484±0.222
J22114+409	1RXS J221124.3+410000	M5.5 V	0.638±0.555	0.494±0.985	0.602±0.103	2907±105	0.175±0.066	-2.644±0.223
J22115+184	GJ 851	M2.0 V	2.758±0.149	2.374±0.294	3.867±0.179	3571±102	0.464±0.066	-1.473±0.220
J22125+085	GJ 9773	M3.0 V	2.971±0.195	2.524±0.375	2.071±0.167	3479±108	0.374±0.067	-1.796±0.224
J22137-176	GJ 1265	M4.5 V	1.150±0.392	1.535±0.772	1.129±0.121	3045±114	0.216±0.068	-2.487±0.229
J22252+594	GJ 4276	M4.0 V	2.088±0.255	1.307±0.542	2.182±0.160	3304±126	0.352±0.067	-1.790±0.224
J22298+414	GJ 1270	M4.0 V	1.679±0.277	2.158±0.566	0.588±0.117	3135±111	0.241±0.067	-2.219±0.227
J22330+093	GJ 863	M1.0 V	3.074±0.277	2.832±0.541	3.242±0.304	3573±112	0.429±0.068	-1.637±0.228
J22468+443	GJ 873	M3.5 V	1.312±0.257	2.024±0.518	1.281±0.191	3087±108	0.228±0.067	-2.455±0.225
J22503-070	GJ 875	M0.5 V	4.021±0.151	3.270±0.348	4.309±0.223	3835±112	0.546±0.068	-1.280±0.229
J22518+317	GJ 875.1	M3.0 V	0.794±0.237	0.893±0.477	1.606±0.300	3038±109	0.237±0.067	-2.288±0.225

(continued on next page ..)

Table B1 – continued from the previous page.

Karmn ^(a)	Name	Sp.type ^(b)	Ca I EW (Å) (0.854 μm)	Ca I EW (Å) (0.866 μm)	Mg I EW (Å) (1.57 μm)	$T_{\text{eff}}^{(c)}$ (K)	Radius ^(c) (R_{\odot})	Luminosity ^(c) ($\log L/L_{\odot}$)
J22532-142	GJ 876	M4.0 V	1.815±0.251	1.847±0.532	1.469±0.193	3202±107	0.275±0.067	-2.193±0.225
J22559+178	GJ 4306	M1.0 V	3.530±0.165	2.827±0.391	4.380±0.272	3750±120	0.534±0.070	-1.283±0.237
J22565+165	GJ 880	M1.5 V	3.153±0.115	2.672±0.273	4.547±0.141	3703±112	0.528±0.068	-1.290±0.228
J23245+578	GJ 895	M1.0 V	3.320±0.147	2.820±0.384	4.763±0.091	3751±107	0.547±0.067	-1.240±0.223
J23340+001	GJ 899	M2.5 V	3.363±0.223	2.469±0.525	3.229±0.224	3629±111	0.462±0.068	-1.488±0.226
J23351-023	GJ 1286	M5.5 V	0.305±0.351	1.053±0.855	0.587±0.253	2849±114	0.141±0.068	-3.004±0.229
J23381-162	GJ 4352	M2.0 V	3.193±0.231	2.790±0.595	2.205±0.141	3533±109	0.392±0.067	-1.745±0.225
J23419+441	GJ 905	M5.0 V	0.456±0.298	0.679±0.807	0.879±0.103	2904±125	0.171±0.069	-2.696±0.231
J23431+365	GJ 1289	M4.0 V	1.876±0.242	1.051±0.624	0.990±0.251	3192±112	0.274±0.068	-2.065±0.227
J23492+024	GJ 908	M1.0 V	2.715±0.091	2.057±0.264	2.853±0.076	3475±104	0.407±0.066	-1.652±0.221
J23505-095	GJ 4367	M4.0 V	1.636±0.397	1.580±0.887	1.835±0.359	3191±128	0.283±0.070	-2.132±0.234
J23556-061	GJ 912	M2.5 V	3.230±0.120	2.580±0.316	3.705±0.300	3639±104	0.478±0.067	-1.447±0.223
J23585+076	GJ 4383	M3.0 V	2.569±0.247	2.279±0.559	1.670±0.167	3373±114	0.333±0.068	-1.939±0.231

Notes. ^(a) Karmn ID are from Reiners et al. (2018). ^(b) Spectral types are from Alonso-Floriano et al. (2015) and references therein. ^(c) T_{eff} , radius and luminosity are estimated in this work using equations (2), (3) and (4) respectively.